

1 **Mineralogical, geochemical, and textural indicators of crystal accumulation in the**

2 **Adamello Batholith (Northern Italy) – Revision 2**

3

4 Alina Maraike Fiedrich*: Department of Earth Sciences, ETH Zurich, 8092 Zurich, Switzerland

5 Olivier Bachmann: Department of Earth Sciences, ETH Zurich, 8092 Zurich, Switzerland

6 Peter Ulmer: Department of Earth Sciences, ETH Zurich, 8092 Zurich, Switzerland

7 Chad D. Deering: Department of Geological and Mining Engineering and Sciences, Michigan

8 Technological University, Houghton, MI 49931, USA

9 Karsten Kunze: Scientific Center for Optical and Electron Microscopy, ETH Zurich, 8093

10 Zurich, Switzerland

11 Julien Leuthold: Department of Earth Sciences, ETH Zurich, 8092 Zurich, Switzerland

12

13 * Corresponding author. telephone: +41 44 632 22 27; e-mail: alina.fiedrich@erdw.ethz.ch

14

15

16

17

18

19

20

21

22

23

Abstract

24

25 In this study, we quantitatively investigate crystal-melt segregation processes in two
26 upper-crustal, intermediate to silicic plutons from the Tertiary Adamello Batholith, Italian Alps,
27 by combining: (a) an estimation of the amount of crystallized interstitial liquid using
28 cathodoluminescence images, phase maps, and mass balance calculations with (b) quantification
29 of crystal preferred orientation using electron back-scatter diffraction. Cathodoluminescence
30 images, phase maps, and plagioclase profiles are used together to distinguish early grown
31 primocrysts from overgrowths formed after the rheological “lock-up” of the magma bodies. Mass
32 balance calculations, taking into account mineral compositions and bulk-rock chemistry, are used
33 as an additional means to quantify the amount of trapped melt. The following features are
34 indicative of crystal accumulation (or melt loss) in some parts of the batholith: (a) The amount of
35 crystallized interstitial liquid can be low and negatively correlated with crystal (and shape)
36 preferred orientations. Locally, up to ca. 27 % melt may have been lost; (b) significant
37 intracrystalline deformation in plagioclase (up to ca. 13° of lattice distortion) is present in
38 strongly foliated samples, resulting from compaction in a highly crystalline mush. These
39 mineralogical and textural features indicative of variability in the degree of crystal accumulation
40 in some areas of the Adamello batholith may explain the highly scattered bulk-rock geochemical
41 patterns (particularly in trace elements). However, the precise quantification of the amount of
42 melt loss remains challenging in felsic plutons, because of the compositional deviation from
43 liquid lines of descent due to multiscale variations in the degree of crystal-melt segregation and
44 the fact that magmatic textures indicative of crystal accumulation can be subtle.

45

46

Key words

47

48 Adamello; crystal cumulate; crystallized interstitial liquid; intermediate to silicic batholith; phase
49 maps; cathodoluminescence

50

51

Introduction

52

Research Interest

54

55 Melt extraction from intermediate to silicic crystal mush has been the topic of numerous studies
56 to explain the origin of crystal-poor rhyolites (e.g. Bacon and Druitt 1988; Hildreth and Fierstein
57 2000; Hildreth 2004; Bachmann and Bergantz 2008; Deering and Bachmann 2010; Huber et al.
58 2012). Most of these studies concentrated on the volcanic products, without clearly linking them
59 to the plutonic record. Yet, the latter retains a more complete (time- and composition-wise)
60 record of the magma reservoir dynamics (see recent publications by Miller and Miller 2002;
61 Turnbull et al. 2010; Paterson et al. 2011; Tappa et al. 2011; Beane and Wiebe 2012; Coint et al.
62 2013; Gutiérrez et al. 2013; Putirka et al. 2014; Graeter et al. 2015; Lee and Morton 2015; Barnes
63 et al. 2016), and can provide important information on the physical mechanisms involved, if any
64 melt segregation has occurred.

65 Melt segregation can be traced by investigating the crystal cumulates left over after melt
66 separation (e.g. Weinberg 2006; Deering and Bachmann 2010). However, the existence of
67 cumulates in intermediate to silicic igneous rocks in the mid- to upper crust is still strongly
68 debated (Bartley et al. 2006; Streck and Grunder 2007; Reubi and Blundy 2009; Deering and
69 Bachmann 2010; Tappa et al. 2011; Davis et al. 2012; Mills and Coleman 2013; Gelman et al.
70 2014; Streck 2014; Glazner et al. 2015; Lee and Morton 2015; issue 4/2016 of “Elements”). If

71 felsic cumulates do not exist, the generation of eruptible melt pockets from shallow, evolved
72 crystal mush, or at least the mechanisms behind it, would be in question. Alternatively, the
73 presence of a significant trapped melt component would render the cumulate signature very
74 subtle (e.g. Gelman et al., 2014).

75 The presence of cumulates in plutonic lithologies may be recorded by the bulk
76 geochemical signature. For example, as concentrations of incompatible trace elements must
77 increase along the liquid line of descent, the greater the melt loss, the stronger the depletion in
78 incompatible trace elements in the final bulk-rock composition. Strong variability in trace
79 element concentrations within a single differentiation series has been reported from individual
80 plutons all over the world (e.g. Lee and Morton 2015; Walker et al. 2015; Eddy et al. 2016), and
81 part of this variability may be related to crystal-melt segregation. However, identification of
82 cumulates utilizing such bulk-rock techniques suffers from the fact that: (a) multiple liquid lines
83 of descent can occur in a single magmatic series, in particular for incompatible elements or
84 elements strongly affected by crustal assimilation, and (b) plutonic lithologies may be
85 compositionally heterogeneous on decimeter to meter scale (coarse-grained lithologies, local melt
86 movement). Hence, to improve our ability to identify the presence of possible intermediate to
87 silicic cumulates, investigations should be extended from (a) analysis of bulk-rock geochemical
88 patterns to (b) quantification of the amount of trapped liquid, which correlates inversely with the
89 amount of melt extraction, and (c) identification of textural indicators of compaction and/or
90 crystal settling (in part summarized in Meurer and Boudreau 1998a; for further references see
91 text below). All three methods complement each other when coupled and provide the most
92 complete image of crystal-melt segregation.

93

94 **Previously applied methods to target the trapped liquid**

95

96 Minerals in magmas grow in a continuum from free-floating crystals in a dominantly liquid
97 environment to interstitial crystals trapped in the pore spaces of highly crystalline mushes. The
98 trapped liquid represents this later phase, originating after the magma has reached the rheological
99 lock-up (ca. 50 vol% crystals, i.e., solid crystal network forms in 3D: Vigneresse et al. 1996;
100 Petford 2003; Dufek and Bachmann 2010). Estimation of the amount of trapped liquid has been
101 attempted for several magmatic systems by means of bulk-rock geochemistry and trace element
102 modeling in mafic rocks (e.g., Bédard 1994; Meurer and Boudreau 1998a and references therein;
103 Tegner et al. 2009; Leuthold et al. 2014) and in silicic rocks (e.g., McCarthy and Groves 1979;
104 Deering and Bachmann 2010; Gelman et al. 2014; Lee and Morton 2015). The accuracy of such
105 trace element based models depends on the choice of partition coefficients and/or starting
106 compositions, which can vary significantly in many cases. Partition coefficients and the modal
107 mineralogy can vary as a function of pressure, temperature, and melt composition (Blundy and
108 Wood 2003; Forni et al. 2016; although, time-integrated partition coefficients can be internally
109 estimated with high confidence, e.g., Otamendi et al. 2016), while starting compositions cannot
110 be assumed to be perfectly constant nor precisely determined, especially in large magmatic
111 provinces. In addition, averaging of many samples is required to obtain partition coefficients
112 representative for a large plutonic body, but this also impedes the study of variability across the
113 pluton.

114 Other techniques that have been utilized to estimate the amount of trapped liquid focused
115 more on mineralogical and textural constraints. For example, Graeter et al. (2015) utilized
116 energy-dispersive x-ray spectroscopy (EDS) compositional maps to determine phase proportions
117 and the amount of low-anorthite overgrowth rims on plagioclase in felsic plutonic rocks. A
118 number of studies applied cathodoluminescence (CL) imaging to visualize phase proportions

119 (Higgins 2016) and stages of growth in minerals such as quartz or feldspar (e.g. Wiebe et al.
120 2007, Müller et al. 2010, Götze 2012, Vasyukova et al. 2013, Frelinger et al. 2015). Furthermore,
121 CL is commonly combined with other tools such as crystal-size distributions (Higgins 2016),
122 quantitative trace element analysis (e.g. Müller et al. 2003, Słaby et al. 2016), or geochemical
123 modelling (Słaby and Götze 2004) to elucidate the crystallization history. Ginibre (2002, 2007)
124 and Perugini et al. (2005) applied combined back-scatter electron (BSE) imaging and electron
125 probe micro-analysis to reconstruct the conditions that gave rise to different growth zones in
126 feldspars, thereby providing an alternative method to determine overgrowth rims. In all cases,
127 variations within units can be explored, and the results can be coupled with textural information.
128 However, separating “cores” (crystals in a largely liquid environment) from “rims” (parts of the
129 crystals that grow from trapped melt in the pore space) of crystals remains challenging, as
130 multiple variables (e.g., temperature, water content, pressure, degree of differentiation) can have
131 an effect on the compositional parameters (e.g., anorthite content in plagioclase).

132 Cumulate textures are frequently reported from mafic to ultramafic rocks (e.g., Wager
133 1960; Brothers 1964; Hunter 1996; Namur and Charlier 2012) but only rarely in intermediate to
134 silicic rocks (e.g. Lee and Morton 2015). This is likely due to the higher viscosity of the evolved
135 magma, which leads to a less efficient separation between crystals and melt (Bachmann et al.
136 2007). Additional factors may be the cooling rate, the relative density difference between crystals
137 and melt, crystal size and crystal shape (e.g. Brothers 1964). Possible textural indicators of
138 crystal accumulation and melt segregation are magmatic foliation (e.g., Brothers 1964; Hunter
139 1996; Meurer and Boudreau 1998b, 1998a their Table 2; Namur and Charlier 2012),
140 intracrystalline deformation (Hunter 1996; Philpotts et al. 1996; Meurer and Boudreau 1998b;
141 Philpotts and Philpotts 2005), and crystal clusters (“synneusis”: Vance 1969; Schwindinger and
142 Anderson 1989; Philpotts et al. 1998, 1999; Jerram et al. 2003; Beane and Wiebe 2012; Graeter

143 et al. 2015).

144 Several ways to quantify the development of these types of igneous textures have been
145 developed (e.g., Launeau and Robin 1996; Meurer and Boudreau 1998b; Launeau et al. 2010).
146 Recently, improvement of the electron back-scatter diffraction (EBSD) systems has enabled rapid
147 crystal orientation mapping (Wheeler et al. 2001). Crystal preferred orientation (CPO) is now
148 commonly quantified based on orientation data from EBSD measurements by means of the
149 "J-index" (Bunge 1982; Ben Ismaïl and Mainprice 1998) or the "misorientation (M)-index"
150 (Skemer et al. 2005; Mainprice et al. 2014). Here, CPO and shape preferred orientation (SPO) are
151 equivalent, but for simplicity and because EBSD measures crystal orientations, we use the term
152 "CPO" to describe both CPO and SPO in the following.

153

154 **Purpose of this study**

155

156 Transcrustal igneous systems featuring evolved, upper-crustal crystal mushes still defy our
157 understanding (see recent reviews in Bachmann and Huber 2016; Cashman et al. 2017). In an
158 effort to determine, if the origin of the large scatter observed in many bulk-rock geochemical
159 datasets for plutonic systems is related to variability in the efficiency of crystal-melt separation,
160 we assessed cumulate characteristics in carefully chosen lithologies of the Adamello batholith.
161 Phase maps from energy-dispersive x-ray spectroscopy (EDS) scans and cold-cathode CL images
162 were obtained to determine the amount of trapped liquid in different parts of the batholith. The
163 results were compared with those from trace element mass balance calculations, as performed in
164 Leuthold et al. (2014).

165 Crystal orientations and crystal deformation measured with EBSD were used to
166 characterize and quantify fabrics, which could be further used to determine the underlying

167 magmatic processes. In particular, we focused on identifying crystal-liquid separation
168 mechanisms that might have occurred and are likely to fall into one or several of the following
169 categories: (a) hindered settling (Davis and Acrivos 1985; Bachmann and Bergantz 2004; Beane
170 and Wiebe 2012; Lee and Morton 2015), (b) compaction (McKenzie 1984, 1985; Shirley 1986;
171 Philpotts et al. 1996; Jackson et al. 2003; Bachmann and Bergantz 2004; Philpotts and Philpotts
172 2005), (c) micro-settling (Miller et al. 1988), and (d) gas-driven filter-pressing (Anderson et al.
173 1984; Sisson and Bacon 1999; Bachmann and Bergantz 2006; Pistone et al. 2015). In a nutshell,
174 we applied a range of techniques to determine whether evidence for crystal-melt segregation in
175 intermediate to silicic plutonic systems is preserved.

176

177

Geological setting

178

179 The Adamello batholith is a ca. 42 to 31 Ma (Del Moro et al. 1983b; Mayer et al. 2003;
180 Schaltegger et al. 2009) Alpine intrusion (Brack 1983), located in the Southern Alps of Northern
181 Italy (Figure 1a). It intruded into crystalline basement of the Southern Alps and the
182 Permo-Mesozoic cover sediments (Brack 1983) and is wedged between the Periadriatic (Insubric)
183 fault system (Figure 1a; Laubscher 1983). Paleo-intrusion pressure is less than 3.5 kbar
184 (Thompson et al. 2002; Pennacchioni et al. 2006 and references therein). Today, the batholith is
185 well-exposed over an area of ca. 670 km² and shows > 2 km of vertical relief. The dominant rock
186 types are tonalite and granodiorite (Brack 1983). Potential hints to volcanic activity related to the
187 Adamello batholith are rare and ambiguous (Boyet et al. 2001; Martin and Macera 2014).

188 Emplacement of the plutons of the Adamello batholith in the upper crust occurred
189 incrementally (see, for example, separation of units by sharp contacts in Figure 1; Schaltegger et

190 al. 2009; Schoene et al. 2012; Floess and Baumgartner 2015) and under predominantly
191 extensional tectonic conditions (Brack 1983; Callegari 1983; Laubscher 1983). The plutons
192 originated from a mantle-derived, Mg-tholeiitic to high-Mg basaltic parental magma (Ulmer et al.
193 1983; Bigazzi et al. 1986; Kagami et al. 1991; Hürlimann et al. 2016) that underwent progressive
194 crustal assimilation and fractional crystallization (AFC; Taylor 1980). Fractionation followed a
195 calc-alkaline, I-type trend (Macera et al. 1983), which is typical for subduction-related magmas.
196 Geologically and lithologically similar occurrences of composite batholiths are known from most
197 continental arcs and are summarized in Lipman & Bachmann (2015).

198 The Adamello batholith *sensu lato* consists of four composite plutons (also referred to as
199 superunits) younging from southwest to northeast (Del Moro et al. 1983b; Callegari and Brack
200 2002): Re di Castello (including Corno Alto), Adamello (including the Western Adamello
201 Tonalite, WAT), Avio - Val di Genova, and Presanella (Figure 1a). The homogeneity and volume
202 of batches increase with younging (compare to Figure 1a; for WAT: Floess and Baumgartner
203 2015), possibly indicating progressive heating of the crust, while the mantle source may vary
204 slightly (Macera et al. 1983; Hürlimann et al. 2016). Progressive heating is accompanied by an
205 apparent increase in assimilation with time, which is indicated by higher $^{87}\text{Sr}/^{86}\text{Sr}$ ratios and $\delta^{18}\text{O}$
206 values in the younger superunits (Cortecci et al. 1979; Del Moro et al. 1983a). Detailed
207 summaries of research on the Adamello batholith are presented in Bianchi et al. (1970), Brack
208 (1983), Callegari (1983), and Callegari and Brack (2002).

209 Re di Castello (sampling area 1) is the best studied of the four superunits. The
210 emplacement age is ca. 42.4 Ma to 40.9 Ma, yielding an intrusion span of ca. 1.5 Myr
211 (Schaltegger et al. 2009). This superunit comprises the largest proportion of mafic material (see
212 Figure 1). Incremental growth with repose times long enough for sharp contacts to develop
213 between some batches (Schaltegger et al. 2009; Brack 1983) is evident particularly in the

214 southern part. In this contribution, we focused on the magma batches “Avortici”, “Spotty Dog”,
215 and “Vacca” from the Lago della Vacca complex (Figure 1b; as defined in John and Blundy
216 1993). For simplification, these three batches together are referred to as “LdV” in the following.
217 Sharp contacts in the Lago della Vacca complex exist between “Blumone”, “Vacca” and
218 “Galliner Granodiorite” (Figure 1b; as defined, e.g., in Ulmer et al. 1983). Between “Spotty dog”
219 (SD) and “Avortici” (AV) (Figure 1b), for example, discernible magma batches show diffuse,
220 curvy contacts and mingling. Heterogeneities in the studied batches comprise, for example, thin,
221 leucocratic bands depleted in dark minerals, deformed mafic enclaves (Figure 2a), and xenoliths.
222 The development of a pronounced planar fabric within these batches likely occurred
223 synchronously with magma intrusion (John and Blundy 1993). The samples studied in more
224 detail (Ada14-AVx) are from “Avortici”.

225 Western Adamello Tonalite (WAT, sampling area 2) is one of the two discernible batches
226 of the Adamello superunit, and was emplaced within ca. 1.2 Myr, from ca. 37.6 Ma to 36.4 Ma
227 (Floess and Baumgartner 2015). In contrast to LdV, WAT is mainly composed of largely
228 homogeneous tonalite and possesses only minor amounts of gabbro, along its border (Callegari
229 1983). It appears heterogeneous on a decimeter- to meter-scale. For example, it exhibits: (a)
230 biotite-hornblende-dominated crystal clots of up to a few mm in diameter, (b) abundant
231 fine-grained dioritic to gabbroic enclaves, which most likely originate from dikes that were
232 injected into and mingled with the crystal mush, (c) some pieces of mafic cumulate, (d) rare
233 xenoliths of crustal origin, and (e) leucocratic bands (centimeter to decimeter thick) that are
234 variably depleted in biotite and hornblende and show diffuse to sharp transitions into their host
235 tonalite (Figure 2b). Pervasive foliation is characteristic for the Southern “External Zone” of
236 WAT, which was interpreted as a conduit that transported magma upward (Floess and
237 Baumgartner 2015), but is rare in sampling area 2, which is part of the “Internal Zone” (Floess

238 and Baumgartner 2015). The samples studied in more detail (Ada14-AFx) are derived from the
239 “Internal Zone” of WAT.

240

241

Methodology

242

Bulk-rock and mineral chemistry

244

245 Major element compositions of the bulk-rock were determined by x-ray fluorescence (XRF)
246 spectroscopy on fused glass beads, with a PANalytical Axios XRF spectrometer at the
247 Department of Earth Sciences, ETH Zurich. An acceleration voltage of 24-60 kV and a current of
248 40-100 mA were applied. Calibration was carried out on 35 internationally accepted standard
249 powders processed to glass beads. The limit of detection is <0.012 wt% for all oxides.

250 Major element compositions of all major phases in four samples (Ada14-AV1a, -AV2,
251 -AF14, and -AF15) were determined for mass balance calculations (aimed at the crystallized
252 liquid fraction). They were measured with a JEOL JXA-8200 electron probe micro-analyzer
253 (EPMA) at the Department of Earth Sciences, ETH Zurich. An acceleration voltage of 15 kV and
254 a beam current of 20 nA were applied, with a spot size of 1-5 μm . Natural and synthetic silicates
255 and oxides were used as standards. Samples were carbon coated (ca. 20 nm thickness).
256 Back-scatter electron images were used in combination with major element profiles across
257 plagioclase and hornblende to distinguish between different zones.

258 Trace element compositions of the bulk-rock and all major mineral phases were
259 determined with laser ablation inductively coupled plasma mass spectrometry (LA-ICP-MS) at
260 the Department of Earth Sciences, ETH Zurich. For the bulk-rock, an Elan 6100 DRC (Perkin
261 Elmer, Canada) mass spectrometer, coupled to a 193 nm ArF Excimer GeoLas (Coherent,

262 Germany) system, was used. Glass beads (of the bulk-rock) were ablated with 90 μm spot size,
263 10 Hz repetition rate, and laser energy density of ca. 12 J/cm^2 . Carrier gas flux was 1.1 L/min He,
264 and auxiliary / sample gas flows were both ca. 0.8 L/min Ar. NIST SRM 610 served as external
265 standard, ablated with 40 μm spot size and an energy density of ca. 5-7 J/cm^2 . Calcium oxide
266 contents (in wt%) from XRF analysis of the bulk-rock served as internal standard. A blank
267 correction was carried out using a blank Li-meta-/tetraborate glass bead. The data from three
268 measurements on each glass bead were averaged to get the bulk-rock concentrations.

269 Trace element analysis was conducted for mass balance calculations. For all major
270 mineral phases except quartz, a Thermo Element XR mass spectrometer connected to a 193 nm
271 Resonetics ArF Excimer laser was used. The laser was operated in a double-volume Laurin
272 Technic S155 ablation cell with a spot size of 19 μm , a repetition rate of 5 Hz and a laser energy
273 density of ca. 3.5 J/cm^2 . Carrier gas flow was 0.7 L/min He, and auxiliary / sample gas flows
274 were both ca. 1.0 L/min Ar. Major element data from EPMA were used as internal standards,
275 NIST SRM610 for external standardization and GSD-1G basalt glass as a secondary standard.
276 Trace elements in quartz were measured with the same instrument and setup as for bulk-rock
277 trace elements, except that the laser energy density was higher (ca. 13-16 J/cm^2), and SiO_2
278 content (set as 99.9 wt.%) was used as internal standard. The Matlab-based software SILLS
279 (Guillong et al., 2008b) was used for data reduction, including time-dependent instrumental drift,
280 gas blank and relative sensitivity corrections, for the bulk-rock and all major phases.

281

282 **Cathodoluminescence imaging**

283

284 Cathodoluminescence (CL) images were obtained on an ERI-MRTech optical CL microscope
285 with a cold cathode mounted on an Olympus BX41 petrographic microscope at the University of

286 Geneva. Acquisition conditions were: gun current of ca. 300 μA , high voltage of ca. 11 kV,
287 defocused beam with a diameter of ca. 1 cm, residual pressure of ca. 50 mTorr. Samples were
288 uncoated and the chamber was flushed with Ar.

289

290 **Phase and plagioclase maps**

291

292 Energy-dispersive X-ray spectroscopy (EDS) scanning was applied to obtain compositional maps
293 of thin sections. For EDS scans and spot analyses, thin sections were coated with a ca. 20 nm
294 thick carbon layer. Ten EDS maps were produced using a *Jeol JSM-6390LA* instrument at the
295 Department of Earth Sciences, ETH Zurich, equipped with a *Thermo Fisher Ultradry* EDS
296 detector coupled to a *Thermo Fisher Noran System 7* and (a) an LaB_6 filament or (b) a Tungsten
297 filament. An acceleration voltage of 15 kV was applied. Scanning mode was ten frames for 60 s
298 each with 22700 counts per second, and a resolution of 128x96 pixels, resulting in a step size of
299 ca. 20 μm .

300 Phase maps and plagioclase maps (plagioclase was selected because of its variable
301 composition and broad crystallization interval) were created with the *PARC*-based spectral image
302 processing software *iSpectra* (Liebske 2015), written in *WaveMetrics' Igor Pro*. Area% was
303 directly converted to volume%, i.e. these were assumed to be equal.

304 An error of up to a few percent for most phases is introduced by direct conversion from
305 area% to volume%, as a comparison between the results from phase maps and *CIPW* norm
306 (Kesley 1965; Cox et al. 1979) revealed. This is acceptable for at least the major phases quartz,
307 plagioclase, alkali feldspar, and probably hornblende. It may, however, introduce a larger error
308 for platy minerals such as biotite in foliated samples. Reliability of the estimates of the phase
309 proportions can be improved through scans over a larger area, which is particularly important for

310 coarse-grained samples, and on variably oriented sections through the sample. The stereological
311 basics for conversion were discussed, for example, by Sahagian & Proussevitch (1998), Higgins
312 (2000 and references therein), and Jerram & Higgins (2007). The quantification of anorthite
313 contents by EDS is affected by an error of up to a few percent, with a tendency to produce
314 slightly overestimated anorthite contents (the calibration curve that relates Si/Al intensity ratios
315 with anorthite contents in plagioclase was acquired with slightly different settings for better
316 spectral resolution than the plagioclase maps themselves).

317

318 **Electron back-scatter diffraction**

319

320 Electron back-scatter diffraction (EBSD) measurements on entire thin sections were conducted
321 using a *TESCAN VEGA 3 XLH* scanning electron microscope at the Department of Materials,
322 ETH Zurich. Analysis settings were: sample tilt of 70°, acceleration voltage of 20 kV, high
323 vacuum, working distance of ca. 35 mm. Small-scale EBSD measurements on individual
324 plagioclase crystals were conducted using an *FEI Quanta 200 FEG* scanning electron microscope
325 at the Electron Microscopy Center, ETH Zurich. Analytical settings were as follows: sample tilt
326 of 70°, acceleration voltage of 20 kV, low vacuum of 30 Pa, and working distance of ca. 17 mm.
327 Intracrystalline deformation (bending) of plagioclase was studied through misorientation angles,
328 in two different samples, the foliated sample Ada14-AV1a from LdV and the unfoliated sample
329 Ada14-AF15 from WAT. The error of the EBSD method is often specified to be at least 1° for
330 silicate minerals due to technical limitations (software manual; Prior et al. 1999; Schwartz et al.
331 2009).

332 The program *OIM data collection* by *Ametek-EDAX* was used to acquire EBSD patterns,
333 with a pixel binning of 4x4. Step size was 40 μm for large-scale and 10 μm for small-scale scans.

334 The EBSD measurements were coupled to EDS measurements for better phase assignment and
335 thus more reliable indexing (software option *ChiScan*). The program *OIM Analysis* was used to
336 process the collected data. Indexing files for albite, hornblende, quartz, and orthoclase were used.
337 Filtering for the different phases was based on compositional criteria and adjusted with the
338 software's built-in functions (confidence index and grain size). Grains smaller than 10 pixels
339 were removed; filtering for larger grain sizes (e.g. > 300 pixels) and vice versa does not cause
340 any significant change to the CPO (not presented here).

341 The *Matlab* toolbox *Mtex* (Hielscher and Schaeben 2008; Bachmann et al. 2010) was used
342 to process and analyze the cleaned and filtered EBSD data. Calculation of orientation distribution
343 functions (ODF, Bunge 1982) and quantification of CPO was based on the eigenvalue (Vollmer
344 1990; Mauler et al. 2001; Mainprice et al. 2014). In the following, this approach is termed
345 "Point-Girdle-Random (PGR)" method.

346 Errors in the CPO quantification can be introduced by: (a) variable indexing reliability
347 due to different crystal orientations and (b) variable composition of the mineral phase. The effect
348 of the plagioclase composition on the indexing, however, is assumed to be minor (Lapworth et al.
349 2002; Schwartz et al. 2009, their Figure 26.7).

350

351 **Bulk-rock trace element compositions**

352

353 The two units from Re di Castello displayed in Figure 3 feature trends with significant
354 scatter over a wide range of trace element concentrations. Not only the data for the Re di Castello
355 superunit as a whole (red field) but also for separate units (Val Fredda: red triangles; this unit was
356 selected because of its wide coverage in terms of bulk-rock data in the literature) show significant
357 trace element scatter. The samples studied in more detail also show significant differences in

358 SiO₂ and trace element contents (Figure 3). For a detailed discussion of major element trends see
359 Macera et al. (1983).

360 The magnitude of data scatter may not originate exclusively from open-system processes.
361 We propose that data scatter is enhanced by variable cumulate signatures in the analyzed rock
362 samples (see also Walker et al. 2015; Lee and Morton 2015, for similar interpretations on
363 different plutons), especially where elements change their bulk partition coefficient.

364

365 **Petrography**

366

367 **Texture**

368

369 Textural differences between LdV and WAT were encountered in grain size, shape and lattice
370 preferred orientation, and intracrystalline deformation. Based on the lack of pervasive
371 deformation textures at the scale of the superunits, post-emplacement subsolidus deformation in
372 LdV and WAT is considered weak to absent. Therefore, the features described below relate
373 exclusively to suprasolidus deformation, and, therefore, their relationship to the process of
374 crystal-melt segregation can be examined in detail.

375 Samples from LdV are readily distinguished from those of WAT based on grain size and
376 macroscopic textures. In LdV, grain sizes range between ca. 0.2-4 mm, with the smallest grain
377 sizes encountered in “Avortici” and largest in “Spotty Dog”. Crystal preferred orientation is
378 present, forming a foliation but no pronounced lineation (first described by John and Blundy
379 1993). The intensity of foliations is variable within the studied (sub-) batches. In particular,
380 plagioclase and hornblende crystals are aligned, leaving little pore space that is now filled by
381 biotite, quartz (Figures 4a, 5), alkali feldspar, and late-stage plagioclase (rim). Plagioclase

382 clusters commonly consist of 2-10 crystals, some of which may share narrow, low-anorthite rims.
383 Monomineralic clusters of hornblende and titanite commonly only consist of 2-3 crystals.
384 Samples from "Avortici" and "Spotty Dog" are mostly strongly foliated, whereas the foliation in
385 samples from "Vacca" is weaker. Both plagioclase (Figure 8) and biotite may be bent.
386 Hornblende twins are only rarely bent. Alkali feldspar may show deformation lamellae. Quartz
387 usually shows undulose extinction.

388 Tonalite samples from WAT are significantly coarser grained (ca. 0.5-10 mm), and
389 foliation is absent or subtle. Minerals in WAT are more heterogeneously distributed (e.g.
390 plagioclase crystals may form chain-like networks). Plagioclase clusters occur randomly oriented
391 in chains and as inclusions in large quartz oikocrysts. Clusters in WAT consist of fewer crystals
392 compared to LdV. Large masses of quartz that appear to be individual grains are sometimes
393 actually clusters of several grains, as CL images revealed. Quartz may show some undulose
394 extinction, but evidence for intracrystalline deformation in other minerals is rare.

395

396 **Mineralogy**

397

398 The main minerals in the rock samples, all of which are quartz-diorites to tonalities, are:
399 plagioclase (green in CL: Figure 4), hornblende (non-luminescent, black in CL), quartz (dark
400 blue in CL), and biotite (non-luminescent, black or dark green in CL, if chloritized). Alkali
401 feldspar (turquoise in CL) can only be observed under the microscope. Color indices range from
402 ca. 30 to 40. Samples from LdV are typically more mafic (quartz diorite) compared to those from
403 WAT (tonalite), as they contain more hornblende and plagioclase, and less quartz and alkali
404 feldspar (see section "Comparison of foliated (LdV) and unfoliated (WAT) samples" and Table 1
405 for mineral proportions).

406 Grain shape and mineral inclusions reveal the following crystallization sequence:
407 (pyroxene) > hornblende + plagioclase > biotite + quartz > alkali feldspar, with most minerals
408 crystallizing simultaneously over part of their crystallization interval. This crystallization
409 sequence is supported by experimental work (Nandedkar et al. 2014). It is clearest for LdV but
410 assumed to also apply to WAT.

411 Hornblende is relatively large (ca. 3 mm in Avorticci to ca. 10 mm in WAT), euhedral to
412 subhedral, and hosts randomly oriented plagioclase inclusions (John and Blundy 1993), apatite
413 (yellow in CL), opaque minerals, and biotite flakes (the latter likely being near-solidus reaction
414 products). Moreover, hornblende in LdV exhibits color zoning from a brown core to green rim
415 (visible in transmitted light mode). In WAT, however, brown hornblende appears to be absent (or
416 much rarer).

417 Plagioclase is euhedral to subhedral, the most abundant mineral in all studied samples,
418 and can have inclusions of hornblende and opaque minerals. Its morphology is tabular (in LdV)
419 to stubby columnar (in WAT). It forms a mostly equigranular texture with a few exceptionally
420 large (>1 cm) crystals. Albite, Carlsbad, and Pericline twinning is frequent. Zoning can be
421 summarized as follows (Supplemental data file 2): (a) cracked, inner core of anorthite > 80, (b)
422 outer core, characterized by pronounced oscillatory zoning between ca. 75-45 anorthite and less
423 or no oscillatory zoning between ca. 50-40 anorthite, and (c) normally zoned rim of anorthite \leq
424 40 (Figure 4b – light green to brown-green in CL, Figure 5; Supplemental data file 2), in textural
425 equilibrium with green hornblende rim, quartz, and biotite. The common brown-green rims (in
426 CL) of plagioclase (Figure 4b) likely correspond to low-anorthite rims quantified with phase
427 maps (see below). Partly altered and fractured, inner cores are common in LdV (Figures 4a –
428 bright green in CL, 5) and rare or absent in WAT. Apart from high-anorthite inner cores, EPMA
429 core-rim profiles show similar patterns (Supplemental data file 2) in samples from LdV and

430 WAT.

431 Biotite and quartz crystals are larger and more abundant in WAT and “Vacca” than in
432 “Avortici” and “Spotty Dog” (see section “Comparison of foliated (LdV) and unfoliated (WAT)
433 samples”, Table 1). Biotite and quartz are anhedral in “Avortici” and “Spotty Dog” and anhedral
434 to subhedral in WAT and “Vacca”. Biotite may be partly chloritized (Figure 4a - dark green in
435 CL).

436 Quartz reveals a mostly homogeneous color in CL (Figure 4a), which can be attributed to
437 (a) generally low luminescence of quartz that prevents high contrast in cold-cathode CL and/or
438 (b) crystallization without significant variation in luminescence centers (i.e. trace element
439 concentrations). There are rare exceptions of indicated brighter, inner parts of quartz in WAT
440 (Figure 4c). To a large part, however, brightness variations can be attributed to preparation
441 artefacts, underlying non-luminescent minerals, and inclusion trails. Quartz and plagioclase
442 forming myrmekite is common both in LdV and WAT at the interface between plagioclase and
443 alkali feldspar (Figure 4d). The CL color of myrmekite is indistinguishable of that in other
444 plagioclase and quartz.

445 In such medium-K, calc-alkaline intermediate to silicic magmas, alkali feldspar should be
446 the last phase to crystallize (e.g. Tuttle and Bowen 1958). Its anhedral shape as a result of
447 crystallization within the interstices of other minerals (Figure 4a) is evidence of that late growth.
448 Alkali feldspar commonly reveals some color zoning with brighter, euhedral inner parts in CL
449 (Figure 4d).

450 Several other minor phases appear in the samples:

- 451 • Patches of clinopyroxene in hornblende and irregular hornblende clots likely represent
452 relicts of early crystallized clinopyroxene.
- 453 • Apatite is typically an early phase, as it is commonly included in early-crystallizing

454 minerals such as hornblende (Figure 4a).

- 455 • Zircon appears to saturate at intermediate crystallinity, at ca. 60 wt% SiO₂ according to a
456 changing trend in the Zr vs. SiO₂ diagram (not presented here; Supplemental data file 1).
- 457 • Epidote is also present in small quantities, and is interpreted as secondary because its
458 primary stability field does not reach pressures below ca. 5 kbar (NNO, H₂O-saturated;
459 Schmidt and Thompson 1996).

460 Zoning forms in crystals as a result of disequilibrium, which can occur during: (a) simple
461 fractional crystallization, (b) open-system behavior in the form of assimilation of preexisting
462 rocks or magma recharge (Tiepolo et al. 2011), and/or (c) change in pressure-temperature
463 conditions of the magma (e.g. Leuthold et al. 2014). Cracked inner cores of plagioclase, for
464 example, may record an early crystallization history of LdV in a deeper, more mafic reservoir
465 (see also Bachmann and Huber 2016: “polybaric mush model”).

466

467 **Determination of the amount of trapped liquid**

468

469 **Observations from phase and plagioclase maps of foliated (LdV) and non-foliated (WAT)** 470 **samples**

471

472 Samples from LdV and WAT exhibit clearly different mineral proportions (Figure 5), calculated
473 from EDS phase maps. Features associated with plagioclase (Table 1, columns 3-4), which is the
474 dominant phase occurring over > 40 area%, include the following:

- 475 • overlapping, but, on average, lower total percentage of modal plagioclase (Table 1,
476 columns 3-4) in WAT compared to LdV;
- 477 • anorthite contents in plagioclase from WAT and LdV ranging between ca. 90 and 20

478 mol%, with a plateau at 40-60 mol%; common inherited, inner cores with high anorthite
479 (> 80) in LdV (Figure 4);

480 • overlapping percentages of low anorthite (≤ 40) within plagioclase between LdV and
481 WAT (Table 1, column 3; orange-red seams around grains in Figure 5); exceptions are
482 sample VA3 from “Vacca” (LdV), which contains only a low amount of plagioclase with
483 anorthite < 40 but larger amounts of biotite and quartz, and sample Ada14-AF16a3 from
484 WAT.

485 Features associated with all other minerals include the following:

- 486 • highly variable amounts of hornblende (Table 1, column 5), biotite + chlorite (Table 1,
487 column 6), and quartz (Table 1, column 1), with rough correlation between amounts of
488 quartz and [biotite + chlorite];
- 489 • higher hornblende (Table 1, column 5) contents, on average, in LdV (except VA3) than in
490 WAT (in particular, hornblende almost absent in Ada14-AF16a3);
- 491 • significantly greater amounts of quartz and smaller amounts of biotite + chlorite in
492 leucocratic part of one sample from WAT (AF16a3; Table 1, row 9)
- 493 • always small amount of alkali feldspar (Table 1, column 2), and smaller in LdV in
494 comparison to WAT;
- 495 • small amounts of titanite + Fe-oxides (Table 1, column 7) in both cases; titanite tends to
496 be more common in samples from LdV compared to WAT;
- 497 • apatite and zircon present in small amounts in most phase maps but counted together with
498 unindexed pixels (Table 1, column 8) because of uncertain percentages due to the coarse
499 step size and small grain size.

500 Sample Ada14-AV2 from LdV was scanned in three orthogonal orientations to study
501 anisotropy of melt segregation, i.e. of trapped melt distribution, which is a common side-effect of

502 the development of foliation (Hersum 2009). Orthogonal scans yield only small differences in the
503 percentages of high-anorthite plagioclase and hornblende.

504

505 **Minerals contributing to the trapped liquid**

506

507 The trapped liquid is defined as the melt that crystallizes after the magma has reached the
508 rheological lock-up (Vigneresse et al. 1996; Petford 2003; Dufek and Bachmann 2010). Hence, in
509 an idealized system, if no melt extraction has occurred, the upper limit of the amount of trapped
510 liquid should be ca. 50 vol% - ignoring ranges of lock-up crystallinity estimates for simplicity.
511 Any values lower than this are, therefore, assumed to record melt loss i.e. crystal accumulation
512 (in contrast to the crystallized liquid fraction, CLF, as calculated in Meurer and Boudreau 1998a,
513 where 100% correspond to crystallization without loss of melt). The amount and composition of
514 minerals growing after 50 vol% crystallization can be estimated using a presumed crystallization
515 sequence based on existing experimental data under similar conditions on similar bulk-rock
516 compositions (see, for example, classic study by Piwinskii 1973, but also Piwinskii and Wyllie
517 1968; Martel et al. 1999; Scaillet and Evans 1999; Costa et al. 2004; Cadoux et al. 2014;
518 Nandedkar et al. 2014).

519 In the Adamello system, phases that crystallized most likely near the solidus are alkali
520 feldspar, as well as quartz and biotite (although quartz and biotite could have small, likely
521 re-equilibrated primocrystic cores). In contrast, plagioclase and hornblende are high-temperature
522 phases, but capable of growing over a large crystallization interval (Nandedkar et al. 2014), hence
523 having evolved rims that contribute to the trapped liquid. All other phases, including Fe-oxide,
524 titanite, and apatite, are present in amounts < 2 % altogether and likely crystallized early, thus not
525 adding much to the trapped liquid.

526 A “maximum trapped liquid” (Table 2, column 1) was calculated specifically for the
527 Adamello rocks, based on the above constraints. Here, we decided to include all alkali feldspar
528 and quartz, plagioclase with anorthite ≤ 40 (rim), 90 % of the biotite + chlorite (as some may
529 have formed from amphibole), and 5 % of the hornblende (approximate percentage of green rim
530 before partial re-equilibration) in the “maximum trapped liquid”. The results are:

- 531 • In samples from LdV, the “maximum trapped liquid” amounts to 31- 50 %. A “maximum
532 trapped liquid” of 31 % would correspond to a loss of ca. 27 % melt from the parental
533 magma, as no melt loss is assumed to result in 50 % interstitial liquid and complete melt
534 loss with opening of the extraction window at ca. 50 % in 0 % interstitial liquid.
- 535 • In samples from WAT, the “maximum trapped liquid” is ca. 55-62 %. In the leucocratic
536 part of sample Ada14-AF16a from WAT, it is ca. 71 %.

537 In the case of the medium-K Adamello, a “minimum trapped liquid” (Table 2, column 2)
538 can be calculated based on the eutectic phase assemblage that comprises ca. 1 : 1 : 1 of alkali
539 feldspar : quartz : plagioclase (derived from Johannes and Holtz 1996; Johannes 1984; Ehlers
540 1972), assuming that all alkali feldspar is interstitial and crystallized last. Hence, as much quartz
541 and plagioclase as alkali feldspar are assumed to be part of the “minimum trapped liquid”
542 (resulting in plagioclase with an anorthite content of mostly < 30). As MgO and FeO contents are
543 commonly low in near-solidus silicic melts, mafic minerals (e.g., amphiboles) should play only a
544 minor role for late-stage crystallization. Therefore, hornblende and biotite were not included in
545 this “minimum trapped liquid”. Using this technique, we find that the “minimum trapped liquid”
546 estimates do not overlap for LdV and WAT.

- 547 • In samples from LdV, the “minimum trapped liquid” amounts to 6-7 %;
- 548 • In samples from WAT, the “minimum trapped liquid” is at least 12-18 %. In the
549 leucocratic part of sample Ada14-AF16a from WAT, it is at least 20 %.

550 The correlation between “minimum” and “maximum trapped liquid” estimates is positive and
551 nearly linear (Table 2), which indicates that crystal-melt separation occurred predominantly
552 within the main extraction window.

553

554 **Quantification of the crystallized liquid fraction with geochemical modeling**

555

556 Bulk-rock and average major and trace element compositions of the main mineral phases were
557 used together to quantify modal abundances by mass balance (see Supplemental data file 3).
558 Plagioclase inner and outer cores and brown hornblende cores were considered as early crystals,
559 while plagioclase rims, hornblende green rims, quartz, zircon, titanite, magnetite, ilmenite, alkali
560 feldspar, and biotite likely crystallized from the interstitial liquid. Despite its secondary origin
561 (perhaps replacing biotite), epidote was also considered in the mass balance calculation in order
562 to match bulk rock geochemical analyses. Plagioclase-melt partition coefficients for Ba and Sr
563 from Blundy and Shimizu (1991) were used to calculate the composition of the parental magma
564 in equilibrium with plagioclase cores and rims. The chemistry of the parental liquids is assumed
565 to be similar to the Re di Castello basaltic andesitic and andesitic dikes of Hürlimann et al.
566 (2016), which also host: (a) high-anorthite plagioclase inner cores (crystallized at mid- to lower
567 crustal depth), and (b) overgrowth of plagioclase with anorthite content similar to that of the
568 outer core determined in the plagioclase of this study (Hürlimann et al., 2016).

569 The CLF for K and Rb (CLF-K, CLF-Rb; Supplemental data file 3) was calculated with
570 the method of Meurer and Boudreau (1998a). K₂O and Rb are incompatible elements along most
571 of the Adamello liquid line of descent (Figure 3). The Re di Castello basaltic andesitic and
572 andesitic dikes of Hürlimann et al. (2016), that have appropriate Ba and Sr concentrations to
573 match plagioclase core compositions (i.e. ca. 190 < Ba < 450 ppm, 180 < Sr < 600 ppm), contain

574 0.7-1.23 wt% K₂O and 15-43 μg/g Rb. Using the above conditions, sample Ada14-AV1a has a
575 CLF-K of 0.39-0.60 and a CLF-Rb of 0.32-0.58. Using the same parameters, sample Ada14-AV2
576 has a CLF-K of 0.70-1.08 and a CLF-Rb of 0.86-1.53.

577 Samples from WAT are more differentiated than those from LdV, with higher K and Rb
578 concentrations. In contrast to LdV, there is no indication of dikes cross-cutting the WAT. We
579 thus tentatively consider bulk-rock compositions. For samples Ada14-AF14 and -AF15 from
580 WAT, parental melts of intermediate compositions and with higher K and Rb contents (2.1 wt%
581 K₂O and 90 μg/g Rb) were selected. The CLF-K and CLF-Rb calculations yield 0.85-0.91 and
582 0.86-0.91 respectively.

583

584 **Textural indicators for loss of melt**

585

586 **Quantification of the crystal preferred orientation**

587

588 In samples from "Avortici" and "Spotty Dog" from LdV, strong CPO of plagioclase was
589 observed (Figure 6a). The long-axis of crystals in the 2D image are largely subparallel to the long
590 edge of the thin section, and almost all plagioclase crystals in the thin section are connected. Pole
591 figures (Figure 6a) confirm this pronounced foliation: b-axes are aligned perpendicular to the
592 foliation plane visible in the hand specimen, while a- and c-axes are mostly scattered within the
593 foliation plane, roughly perpendicular to the orientation maximum of the b-axes. a- and c-axes
594 show diffuse maxima along the girdles in the pole figures, which indicate a faint lineation.
595 Textural classification based on plagioclase crystal distribution in the foliated sample AV1a from
596 LdV (conducted with CSDcorrections: Higgins 2000, 2002) by means of the "R ratio" (Jerram et
597 al. 1996) yields a value of 1.25 (in the section perpendicular to the foliation), indicating ordered

598 patterns (i.e. the distribution is approaching maximum spacing between each crystal; Clark and
599 Evans 1954). The strong foliation in samples from "Spotty Dog" and "Avortici" (LdV) correlates
600 with only small amounts of "minimum" and "maximum trapped liquid" (Figure 7, Table 2).
601 Sample VA3, representing "Vacca" from LdV, is an exception as its crystals are randomly
602 oriented, but it has a smaller "minimum trapped liquid" than samples from WAT.

603 In contrast, orientation maps of samples from WAT show nearly uniform CPO of
604 plagioclase (Figure 6b). No correlation of orientation with grain sizes could be observed. Crystals
605 in plagioclase chains are randomly oriented. Pole figures and ODFs of samples from WAT
606 highlight the lack of preferred orientation (Figure 6b). Those peaks in orientation distribution that
607 emerge from the ODFs are not consistent between the three axes. The "R ratio" (as described
608 above) for unfoliated sample Ada14-AF15 is 0.87, indicating mostly random distribution with
609 some clustering. The sample from "Vacca" is intermediate in textural character between the other
610 studied batches from LdV and WAT. In the case of samples from WAT, a weak to absent
611 foliation corresponds to large amounts of "minimum" and "maximum trapped liquid" (Figure 7,
612 Table 2).

613

614 **Intracrystalline deformation of plagioclase**

615

616 Intracrystalline deformation was observed in some plagioclase crystals (ca. 5 % with
617 microscopically visible bending) from LdV (Figure 8), predominantly along the long sections
618 (perpendicular to the b-axis) of the grains, whereas samples from WAT did not show any
619 intracrystalline deformation. The diameter of all analyzed crystals or twin domains was < 1 mm
620 (in LdV). Up to ca. 13° misorientation along the long section of the grain was measured, in a
621 grain without indication of subgrain formation. However, grains with more than ca. 5°

622 misorientation commonly already showed the beginning of the development of subgrains. Along
623 the long section of the grains, rotation about different axes was observed. Misorientation angles
624 across grains from LdV are larger than in those from Ada14-AF15 from WAT (close to 0°), even
625 though the grain sizes in LdV are smaller.

626

627

Discussion

628

629 Significance of “minimum” and “maximum trapped liquid” estimates

630

631 The method presented here is aimed at estimating the amount of trapped liquid and targets both
632 the melt separated in the main extraction window between ca. 50-70 % crystallinity (e.g. Dufek
633 and Bachmann 2010) and late-stage extraction (mostly by compaction) close to the solidus
634 (Figure 9). Very good correlation between “minimum” and “maximum trapped liquid” estimates,
635 like in this study (Table 2), indicate that crystal-melt separation occurred predominantly within
636 the main extraction window.

637 The “maximum trapped liquid” estimate is strongly dependent on the crystallization
638 sequence and varies with mineral phases (including anorthite contents) that are allocated to the
639 interstitial liquid. Different samples and magma batches are only comparable, if all followed the
640 same (or very similar) crystallization sequence, starting with similar magma composition.
641 Therefore, reliable results are expected when comparing samples of the same differentiation
642 series. In addition, the selected crystallinity at which the main extraction window should open
643 influences the interpretation. It should also be noted that there is clear evidence of compaction
644 with intracrystalline deformation in LdV, indicating some melt extraction must have occurred
645 beyond the main melt extraction window (as defined in Dufek and Bachmann 2010).

646 The “minimum trapped liquid” is robust against minor variations of the crystallization
647 sequence (and, hence, also of the parental magma composition), as it considers only the eutectic
648 phase assemblage (Figure 9, late stage). Thus, it can be useful where different parental magma
649 compositions preclude meaningful estimates based on the “maximum trapped liquid”. However,
650 the “minimum trapped liquid” may vary not only with the extent of preceding melt extraction, but
651 also with the selected proportions of the eutectic phase assemblage (and late percolation of
652 K-enriched fluids). The selected eutectic composition is simplified and, in reality, depends on
653 melt composition (particularly CaO, K₂O, H₂O content, and peraluminous versus metaluminous
654 melt composition), pressure, and temperature (in the Ab-An-Or diagram: von Platen 1965;
655 Johannes and Holtz 1996).

656

657 **Evidence of crystal accumulation based on the amount of trapped liquid**

658

659 The rock samples from "Avortici" and "Spotty Dog" can be interpreted as cumulates that have
660 formed by different degrees of crystal-melt segregation based on their relatively low amount of
661 “minimum” and “maximum trapped liquid” in combination with strong foliation and
662 intracrystalline deformation. In contrast, CPO and the amount of liquid extraction in WAT
663 samples collected in this study may be small enough to term this magma batch a frozen melt
664 body. The “minimum trapped liquid” in parts of LdV is lower than predicted by Lee & Morton
665 (2015) (always ca. 20-30 vol% trapped in cumulates) and overlaps with the typical amount of
666 intercumulus material in mafic to ultramafic mesocumulates (Irvine 1982). Such low amounts of
667 trapped liquid are partly due to the fact that we do not take into account a large enough volume of
668 rims around primocrysts (particularly plagioclase), but could also be due to some amount of
669 compaction enhancing the melt extraction, as evidenced by intracrystalline deformation.

670 The leucocratic part (Figure 2b) of one sample from WAT, Ada14-AF16a, contains
671 significantly more “maximum trapped liquid” than all other samples. John & Stünitz (1997)
672 suggested that such leucocratic bands were generated by shearing in a deforming crystal mush
673 (see also Caricchi et al. 2007). However, a detailed analysis of such leucocratic bands is beyond
674 the scope of this study.

675 The more mafic character of the studied LdV samples compared to WAT may partly be a
676 result of greater melt loss, although it should be kept in mind that “Avortici” and “Spotty Dog”
677 may have a more primitive parental magma composition than WAT and “Vacca”. The former
678 show less crustal contamination (Del Moro et al. 1983a; Cortecci et al. 1979; Bigazzi et al. 1986)
679 than other batches and may, thus, have had lower initial K₂O and Rb concentration to start with,
680 which in turn would lead to a larger calculated loss of trapped liquid than is actually the case.

681

682 **Integration with bulk-rock trace element matching**

683

684 Results from bulk-rock trace element matching are largely, but not perfectly, in agreement with
685 the estimations of the interstitial liquid from phase maps and CPO, but also highlight the
686 difficulties in identifying and quantifying the interstitial liquid or CLF in intermediate to silicic
687 plutons:

- 688 • Considering any possible parental melt composition, CLF calculations for sample
689 Ada14-AV1a always show melt loss: that is, about 32-60 % of the rock consists of
690 trapped crystallized melt (calculated CLF of ca. 0.32-0.60), and ca. 68-40% (1 – CLF) are
691 cumulus crystals. This is in agreement with strongly developed CPO and low estimates of
692 “minimum” and “maximum trapped liquid”.
- 693 • The calculated CLF for sample Ada14-AV2 is closer to 1, indicating little or no

694 interstitial melt loss. This is in agreement with the lower abundance of cumulus crystals
695 and higher abundance of biotite and quartz compared to sample Ada14-AV1a in phase
696 maps. However, sample Ada14-AV2 is foliated and also contains high-anorthite inner
697 cores of plagioclase.

698 • Estimates of the CLF for samples from WAT are close to 1, indicating a chemistry close
699 to quenched liquid. This is compatible with the absence of foliation, the high modal
700 abundance of quartz, alkali feldspar, and biotite, and the absence of distinct hornblende
701 and plagioclase cores.

702 Calculation of the CLF largely depends on the choice of parental compositions, average
703 trace element contents of minerals, and robust estimation of minerals contributing to the cumulus
704 assemblage or interstitial liquid. Natural dikes in the Re di Castello and bulk-rocks from WAT
705 show large variations in trace element concentrations (Hürlimann et al. 2016; Macera et al. 1983).
706 Consequently, the calculated range of CLF is wide, rendering estimates of melt loss less precise.
707 Moreover, the CLF calculations yield slightly different values depending on the selected element.
708 This also relates to differences in parental magma composition and variable mineral modes.
709 Finally, estimation of the parental liquid chemistry from bulk-rock geochemistry of samples
710 within the studied unit (not dikes), as for samples from WAT, is non-ideal because these may
711 have already lost melt. It has to be kept in mind that, by definition, complete lack of melt loss
712 should yield a CLF of 100 % (Meurer and Boudreau 1998a) and a “maximum trapped liquid” of
713 50 %.

714

715 **Mechanisms generating magmatic foliation**

716

717 Magmatic foliations and intracrystalline deformation of plagioclase are obvious in LdV. Both

718 magmatic flow (near-liquidus) and submagmatic flow (near-solidus) (as defined by Paterson et al.
719 1989) can lead to such textures, assuming no significant subsolidus deformation due to tectonics
720 has occurred. A magmatic mineral fabric was also observed by Turnbull et al. (2010, in the
721 Halfmoon Pluton, New Zealand; see also references therein) and interpreted to have resulted
722 from similar mechanisms as those discussed below.

723 Magmatic flow is an efficient mechanism to generate a fabric due to the higher mobility at
724 relatively low crystallinity. It is featured by crystal rotation without plastic deformation (Paterson
725 et al. 1989) and could be responsible for the orientation of early-crystallized plagioclase and
726 hornblende crystals, and schlieren structures. Magmatic flow may also include marginal upflow
727 of compositionally relatively evolved melt along the magma chamber walls (Spera et al. 1995).
728 This process, although largely rejected in more recent publications (e.g. Bachmann & Bergantz
729 2004), might generate vertical foliation, may lead to crystal-melt segregation, and is potentially
730 most efficient where the magma chamber's sidewalls are steep and vertically extensive (de Silva
731 and Wolff 1995, Spera et al. 1995). However, a pronounced lineation in addition to foliation is
732 usually expected to develop in the course of magmatic flow (e.g. Brothers 1964; Wager and
733 Brown 1968 – for a large number of case studies; Meurer and Boudreau 1998b; Žák et al. 2008).
734 Absence of lineations may be the result of limited flow of the magma or of overprinting by later
735 processes. There are also some cases of magma flow without generation of lineation documented
736 (Higgins 1991; Nicolas 1992).

737 Submagmatic flow, on the contrary, lacks suspension-like behavior but still takes place
738 under suprasolidus conditions (Paterson et al. 1989). Mechanisms operating in this flow regime
739 (Paterson et al. 1989; Meurer and Boudreau 1998b) that can generate planar fabrics are hindered
740 settling and compaction (e.g. McKenzie 1984, 1985; Davis and Acrivos 1985; Bachmann and
741 Bergantz 2004; Lee and Morton 2015). It is expected that all magmas go through a phase of

742 hindered settling (indicated, for example, by crystal clusters; Graeter et al. 2015), and can then
743 transition into a compaction stage, if viscosities are low enough, and cooling rates slow enough.
744 Some compaction has apparently occurred in LdV, as the observed deformation (bending,
745 development of deformation twins, and kinking of crystals) implies. However, compaction is
746 slow in shallow silicic systems (McKenzie 1985; Wickham 1987; Bachmann and Bergantz 2004;
747 Lee and Morton 2015). Therefore, it should not generate strong foliation (e.g. Higgins 1991) and
748 may not have generated much additional melt extraction.

749 Development of foliation and compaction features were likely reinforced by magma
750 emplacement through ballooning (e.g. Holder 1979) in the case of LdV (John and Blundy 1993;
751 Schoene et al. 2012). Strong evidence for forceful injection of magma batches before
752 solidification of precursor batches was provided by John and Blundy (1993) on the basis of
753 extensive strain measurements.

754

755

Implications

756

757 Understanding the volcanic-plutonic connection is one of the most prominent research topics in
758 igneous petrology (Bachmann et al. 2007; Lipman 2007; Glazner et al. 2008; Annen 2009; Huber
759 et al. 2012; Cashman and Sparks 2013; “Elements” issue 4/2016 on the “Enigmatic Relationship
760 Between Silicic Volcanic and Plutonic Rocks”; Bachmann and Huber 2016; Cashman et al.
761 2017). The study of melt extraction from highly crystalline magma reservoirs (crystal mush) is
762 key in understanding crustal differentiation and does not only contribute to geochemical
763 diversity, but is also the logical first step in generating volcanic rocks from magma chambers.

764 Reliable evidence for crystal accumulation in plutonic lithologies includes magmatic
765 foliation, crystal bending, and relatively low amounts of trapped liquid. The method presented in

766 this paper is able to resolve variability in melt extraction within a pluton that was relatively
767 homogeneous upon emplacement; estimation of volumes of melt extracted from mushy reservoirs
768 is more robust, if the parental melt composition and crystallization sequence are well known. If
769 this is not the case, we argue that relative differences in crystal-melt segregation may still be
770 resolvable through the abundance of the eutectic phase assemblage (“minimum trapped liquid”
771 fraction” (see Figure 9 for conceptual model).

772 Assessment of the significance of the data presented here with respect to entire batholiths
773 requires more systematic, dense sampling over a larger area of the plutons to study, e.g., how
774 consistent the textures are on a larger scale and how robust the correlation between texture and
775 trapped melt is. Hence, further studies should look at the largest possible number of samples with
776 variable texture strength from a coherent differentiation series. Moreover, a combination of
777 different approaches, which provide different pieces of evidence for crystal-melt segregation, is
778 key to assess the relative contributions of different mechanisms, such as hindered settling,
779 compaction, and filter-pressing. For example, the correlation between CPO and amount of
780 trapped liquid observed in our study may imply that deformation during crystallization of crystal
781 mushes is an efficient way to extract interstitial liquid (e.g. by Caricchi et al. 2007).

782

783

Acknowledgements

784

785 This research was supported by SNF fund # 200020_165501 to O. Bachmann. We thank
786 Christian Liebske (extensive computational support with iSpectra), Lydia Zehnder, and Markus
787 Wälle (XRF measurements and support at LA-ICP-MS, respectively, for samples analyzed in the
788 course of this project). Thanks to Dina Klimentyeva for EPMA and LA-ICP-MS analyses of
789 minerals. Access to SEM-EBSD systems at ETH Zurich (Laboratory for Nanometallurgy and

790 ScopeM) is acknowledged. We also thank Felix Marxer and Maren Wanke for discussions and
791 literature suggestions and Ben Ellis and Meredith Townsend for comments on an earlier version
792 of this manuscript. J. Leuthold (responsible for CLF calculations) acknowledges support from
793 a Swiss National Science Foundation (SNSF) Ambizione grant.

794

795

796

Reference list

797

- 798 Anderson, A.T.J., Swihart, G.H., Artioli, G., and Geiger, C.A. (1984) Segregation vesicles, gas
799 filter-pressing, and igneous differentiation. *The Journal of Geology*, 55–72.
- 800 Annen, C. (2009) From plutons to magma chambers: Thermal constraints on the accumulation of eruptible
801 silicic magma in the upper crust. *Earth and Planetary Science Letters*, 284, 409–416.
- 802 Bachmann, F., Hielscher, R., and Schaeben, H. (2010) Texture Analysis with MTEX – Free and Open
803 Source Software Toolbox. *Solid State Phenomena*, 160, 63–68.
- 804 Bachmann, O., and Bergantz, G. (2004) On the Origin of Crystal-poor Rhyolites: Extracted from
805 Batholithic Crystal Mushes. *Journal of Petrology*, 45, 1565–1582.
- 806 ——— (2006) Gas percolation in upper-crustal silicic crystal mushes as a mechanism for upward heat
807 advection and rejuvenation of near-solidus magma bodies. *Journal of Volcanology and*
808 *Geothermal Research*, 149, 85–102.
- 809 ——— (2008) The magma reservoirs that feed supereruptions. *Elements*, 4.1, 17–21.
- 810 Bachmann, O., and Huber, C. (2016) Silicic magma reservoirs in the Earth’s crust. *American*
811 *Mineralogist*, 101, 2377–2404.
- 812 Bachmann, O., Miller, C.F., and de Silva, S.L. (2007) The volcanic–plutonic connection as a stage for
813 understanding crustal magmatism. *Journal of Volcanology and Geothermal Research*, 167, 1–23.
- 814 Bacon, C.R., and Druitt, T.H. (1988) Compositional evolution of the zoned calcalkaline magma chamber
815 of Mount Mazama, Crater Lake, Oregon. *Contributions to Mineralogy and Petrology*, 98, 224–
816 256.
- 817 Barnes, C.G., Coint, N., and Yoshinobu, A. (2016) Crystal accumulation in a tilted arc batholith.
818 *American Mineralogist*, 101, 1719–1734.
- 819 Bartley, J.M., Coleman, D.S., and Glazner, A.F. (2006) Incremental pluton emplacement by magmatic
820 crack-seal. *Earth and Environmental Science Transactions of the Royal Society of Edinburgh*, 97,
821 383–396.

- 822 Beane, R., and Wiebe, R.A. (2012) Origin of quartz clusters in Vinalhaven granite and porphyry, coastal
823 Maine. *Contributions to Mineralogy and Petrology*, 163, 1069–1082.
- 824 Bédard, J.H. (1994) A procedure for calculating the equilibrium distribution of trace elements among the
825 minerals of cumulate rocks, and the concentration of trace elements in the coexisting liquids.
826 *Chemical Geology*, 118, 143–153.
- 827 Ben Ismail, W., and Mainprice, D. (1998) An olivine fabric database: an overview of upper mantle fabrics
828 and seismic anisotropy. *Tectonophysics*, 296, 145–157.
- 829 Bianchi, A., Callegari, E., and Jobstraibizer, P.G. (1970) I tipi petrografici fondamentali del Plutone
830 dell'Adamello. Tonaliti, quarzodioriti, granodioriti e loro varietà leucocrate. *Mem Ist Geol Min*
831 *Univ Padova*, 27, 1–148.
- 832 Bigazzi, G., Del Moro, A., and Macera, P. (1986) A quantitative approach to trace element and Sr isotope
833 evolution in the Adamello batholith (northern Italy). *Contributions to Mineralogy and Petrology*,
834 94, 46–53.
- 835 Blundy, J.D., and Shimizu, N. (1991) Trace element evidence for plagioclase recycling in calc-alkaline
836 magmas. *Earth and Planetary Science Letters*, 102.2, 178-197.
- 837 Blundy, J.D., and Sparks, R.S.J. (1992) Petrogenesis of Mafic Inclusions in Granitoids of the Adamello
838 Massif, Italy. *Journal of Petrology*, 33, 1039–1104.
- 839 Blundy, J.D., and Wood, B. (2003) Partitioning of trace elements between crystals and melts. *Earth and*
840 *Planetary Science Letters*, 210, 383–397.
- 841 Boyet, M., Lapiere, H., Tardy, M., Bosch, D., and Maury, R. (2001) Nature des sources des composants
842 andésitiques des Gres du Champsaur et des Gres de Taveyannaz; implications dans l'évolution des
843 Alpes occidentales au Paleogene. *Bulletin de la Société Géologique de France*, 172, 487–501.
- 844 Brack, P. (1983) Multiple intrusions - Examples from the Adamello batholith (Italy) and their significance
845 on the mechanisms of intrusion. *Mem Soc Geol It*, 26, 145–157.
- 846 Broderick, C., Wotzlaw, J.F., Frick, D.A., Gerdes, A., Ulianov, A., Günther, D., and Schaltegger, U.
847 (2015) Linking the thermal evolution and emplacement history of an upper-crustal pluton to its
848 lower-crustal roots using zircon geochronology and geochemistry (southern Adamello batholith,
849 N. Italy). *Contributions to Mineralogy and Petrology*, 170, 1–17.
- 850 Brothers, R.N. (1964) Petrofabric Analyses of Rhum and Skaergaard Layered Rocks. *Journal of*
851 *Petrology*, 5, 255–274.
- 852 Bunge, H.-J. (1982) *Texture analysis in materials science: mathematical methods*, 593 p. Butterworths,
853 London, UK.
- 854 Cadoux, A., Scaillet, B., Druitt, T.H., and Deloule, E. (2014) Magma storage conditions of large Plinian
855 eruptions of Santorini Volcano (Greece). *Journal of Petrology*, 55, 1129–1171.
- 856 Callegari, E. (1983) Geological and petrological aspects of the magmatic activity at Adamello (Northern
857 Italy). *Mem Soc Geol It*, 26, 83–103.
- 858 Callegari, E., and Brack, P. (2002) Geological map of the Tertiary Adamello batholith (Northern Italy) -

- 859 Explanatory notes and legend. *Mem Sci Geol*, 54, 19–49.
- 860 Caricchi, L., Burlini, L., Ulmer, P., Gerya, T., Vassalli, M., and Papale, P. (2007) Non-Newtonian
861 rheology of crystal-bearing magmas and implications for magma ascent dynamics. *Earth and*
862 *Planetary Science Letters*, 264.3, 402-419.
- 863 Cashman, K.V., and Sparks, R.S.J. (2013) How volcanoes work: A 25 year perspective. *Geological*
864 *Society of America Bulletin*, 125, 664–690.
- 865 Cashman, K.V., Sparks, R.S.J., and Blundy, J.D. (2017) Vertically extensive and unstable magmatic
866 systems: A unified view of igneous processes. *Science*, 355.6331, eaag3055.
- 867 Clark, P.J., and Evans, F.C. (1954) Distance to nearest neighbor as a measure of spatial relationships in
868 populations. *Ecology*, 35, 445–453.
- 869 Coint, N., Barnes, C.G., Yoshinobu, A.S., Barnes, M.A., and Buck, S. (2013) Use of trace element
870 abundances in augite and hornblende to determine the size, connectivity, timing, and evolution of
871 magma batches in a tilted batholith. *Geosphere*, 9, 1747–1765.
- 872 Cortecchi, G., Del Moro, A., Leone, G., and Pardini, G.C. (1979) Correlation between strontium and
873 oxygen isotopic compositions of rocks from the Adamello Massif (Northern Italy). *Contributions*
874 *to Mineralogy and Petrology*, 68, 421–427.
- 875 Costa, F., Scaillet, B., and Pichavant, M. (2004) Petrological and Experimental Constraints on the
876 Pre-eruption Conditions of Holocene Dacite from Volcán San Pedro (36°S, Chilean Andes) and
877 the Importance of Sulphur in Silicic Subduction-related Magmas. *Journal of Petrology*, 45, 855–
878 881.
- 879 Cox, K.G., Bell, J.D., and Pankhurst, R.J. (1979) *The interpretation of igneous rocks*, 450 p. George,
880 Allen and Unwin, London.
- 881 Davis, J.W., Coleman, D.S., Gracely, J.T., Gaschnig, R., and Stearns, M. (2012) Magma accumulation
882 rates and thermal histories of plutons of the Sierra Nevada batholith, CA. *Contributions to*
883 *Mineralogy and Petrology*, 163, 449–465.
- 884 Davis, R.H., and Acrivos, A. (1985) Sedimentation of Noncolloidal Particles at Low Reynolds Numbers.
885 *Annual Review of Fluid Mechanics*, 17, 91–118.
- 886 De Campos, C.P., Dingwell, D.B., Perugini, D., Civetta, L., and Fehr, T.K. (2008) Heterogeneities in
887 magma chambers: insights from the behavior of major and minor elements during mixing
888 experiments with natural alkaline melts. *Chemical Geology*, 256.3, 131-145.
- 889 Deering, C.D., and Bachmann, O. (2010) Trace element indicators of crystal accumulation in silicic
890 igneous rocks. *Earth and Planetary Science Letters*, 297.1, 324–331.
- 891 Del Moro, A., Ferrara, G., Tonarini, S., and Callegari, E. (1983a) Rb-Sr systematics on rocks from the
892 Adamello batholith (Southern Alps). *Mem Soc Geol It*, 26, 261–284.
- 893 Del Moro, A., Pardini, G., Quercioli, C., Villa, I.M., and Callegari, E. (1983b) Rb/Sr and K/Ar chronology
894 of Adamello granitoids, Southern Alps. *Mem Soc Geol It*, 26, 285–299.
- 895 De Silva, S.L., and Wolff, J.A. (1995) Zoned magma chambers: the influence of magma chamber

- 896 geometry on sidewall convective fractionation. *Journal of Volcanology and Geothermal Research*,
897 65.1-2, 111-118.
- 898 Dufek, J., and Bachmann, O. (2010) Quantum magmatism: Magmatic compositional gaps generated by
899 melt-crystal dynamics. *Geology*, 38.8, 687–690.
- 900 Eddy, M.P., Bowring, S.A., Miller, R.B., and Tepper, J.H. (2016) Rapid assembly and crystallization of a
901 fossil large-volume silicic magma chamber. *Geology*, 44, 331–334.
- 902 Ehlers, E.G. (1972) *The interpretation of geological phase diagrams*, 280 p. Freeman, San Francisco.
- 903 Floess, D., and Baumgartner, L.P. (2015) Constraining magmatic fluxes through thermal modelling of
904 contact metamorphism. Geological Society, London, Special Publications, 422, SP422.8.
- 905 Forni, F., Bachmann, O., Mollo, S., De Astis, G., Gelman, S.E., and Ellis, B.S. (2016) The origin of a
906 zoned ignimbrite: Insights into the Campanian Ignimbrite magma chamber (Campi Flegrei, Italy).
907 *Earth and Planetary Science Letters*, 449, 259–271.
- 908 Frelinger, S.N., Ledvina, M.D., Kyle, J. R., and Zhao, D. (2015) Scanning electron microscopy
909 cathodoluminescence of quartz: Principles, techniques and applications in ore geology. *Ore*
910 *Geology Reviews*, 65, 840-852.
- 911 Gelman, S.E., Deering, C.D., Bachmann, O., Huber, C., and Gutiérrez, F.J. (2014) Identifying the crystal
912 graveyards remaining after large silicic eruptions. *Earth and Planetary Science Letters*, 403, 299–
913 306.
- 914 Ginibre, C., Kronz, A., and Wörner, G. (2002) High-resolution quantitative imaging of plagioclase
915 composition using accumulated backscattered electron images: new constraints on oscillatory
916 zoning. *Contributions to Mineralogy and Petrology*, 142, 436–448.
- 917 Ginibre, C., Wörner, G., and Kronz, A. (2007) Crystal Zoning as an Archive for Magma Evolution.
918 *Elements*, 3, 261–266.
- 919 Glazner, A.F., Bartley, J.M., Coleman, D.S., Gray, W., and Taylor, R.Z. (2004) Are plutons assembled
920 over millions of years by amalgamation from small magma chambers? *GSA today*, 14, 4–12.
- 921 Glazner, A.F., Coleman, D.S., and Bartley, J.M. (2008) The tenuous connection between high-silica
922 rhyolites and granodiorite plutons. *Geology*, 36.2, 183–186.
- 923 Glazner, A.F., Coleman, D.S., and Mills, R.D. (2015) *The Volcanic-Plutonic Connection* pp. 1–22.
924 Springer Berlin Heidelberg.
- 925 Götze, J. (2012) Application of cathodoluminescence microscopy and spectroscopy in geosciences.
926 *Microscopy and Microanalysis*, 18.6, 1270-1284.
- 927 Graeter, K.A., Beane, R.J., Deering, C.D., Gravley, D., and Bachmann, O. (2015) Formation of rhyolite at
928 the Okataina Volcanic Complex, New Zealand: New insights from analysis of quartz clusters in
929 plutonic lithics. *American Mineralogist*, 100, 1778–1789.
- 930 Gutiérrez, F., Payacán, I., Gelman, S.E., Bachmann, O., and Parada, M.A. (2013) Late-stage magma flow
931 in a shallow felsic reservoir: Merging the anisotropy of magnetic susceptibility record with
932 numerical simulations in La Gloria Pluton, central Chile. *Journal of Geophysical Research: Solid*

- 933 Earth, 118, 1984–1998.
- 934 Hawkesworth, C.J., Blake, S., Evans, P., Hughes, R., Macdonald, R., Thomas, L.E., Turner, S.P., and
935 Zellmer, G. (2000) Time Scales of Crystal Fractionation in Magma Chambers—Integrating
936 Physical, Isotopic and Geochemical Perspectives. *Journal of Petrology*, 41, 991–1006.
- 937 Hersum, T. (2009) Consequences of crystal shape and fabric on anisotropic permeability in magmatic
938 mush. *Contributions to Mineralogy and Petrology*, 157, 285–300.
- 939 Hielscher, R., and Schaeben, H. (2008) A novel pole figure inversion method: specification of the MTEX
940 algorithm. *Journal of Applied Crystallography*, 41, 1024–1037.
- 941 Higgins, M.D. (1991) The origin of laminated and massive anorthosite, Sept Iles layered intrusion,
942 Quebec, Canada. *Contributions to Mineralogy and Petrology*, 106.3, 340–354.
- 943 ——— (2000) Measurement of crystal size distributions. *American Mineralogist*, 85, 1105–1116.
- 944 ——— (2002) Closure in crystal size distributions (CSD), verification of CSD calculations, and the
945 significance of CSD fans. *American Mineralogist*, 87, 171–175.
- 946 ——— (2016) Quantitative investigation of felsic rock textures using cathodoluminescence images and
947 other techniques. *Lithos*.
- 948 Hildreth, W. (2004) Volcanological perspectives on Long Valley, Mammoth Mountain, and Mono
949 Craters: several contiguous but discrete systems. *Journal of Volcanology and Geothermal
950 Research*, 136.3, 169–198.
- 951 Hildreth, W., and Fierstein, J. (2000) Katmai volcanic cluster and the great eruption of 1912. *Geological
952 Society of America Bulletin*, 112, 1594–1620.
- 953 Holder, M.T. (1979) An Emplacement Mechanism for Post-Tectonic Granites and Its Implications for
954 Their Geochemical Features. In M.P. Atherton and J. Tarney, Eds., *Origin of Granite Batholiths*
955 pp. 116–128. Birkhäuser Boston.
- 956 Huber, C., Bachmann, O., and Dufek, J. (2012) Crystal-poor versus crystal-rich ignimbrites: A
957 competition between stirring and reactivation. *Geology*, 40, 115–118.
- 958 Hunter, R.H. (1996) Texture Development in Cumulate Rocks. In R.G. Cawthorn, Ed., *Developments in
959 Petrology* Vol. 15, pp. 77–101. Elsevier.
- 960 Hürlimann, N., Müntener, O., Ulmer, P., Nandedkar, R., Chiaradia, M., and Ovtcharova, M. (2016)
961 Primary Magmas in Continental Arcs and their Differentiated Products: Petrology of a
962 Post-plutonic Dyke Suite in the Tertiary Adamello Batholith (Alps). *Journal of Petrology*, 57,
963 495–534.
- 964 Irvine, T.N. (1982) Terminology for layered intrusions. *Journal of Petrology*, 23.2, 127–162.
- 965 Jackson, M.D., Cheadle, M.J., and Atherton, M.P. (2003) Quantitative modeling of granitic melt
966 generation and segregation in the continental crust. *Journal of Geophysical Research: Solid Earth*,
967 108, 2332.
- 968 Jerram, D.A., Cheadle, M.J., Hunter, R.H., and Elliott, M.T. (1996) The spatial distribution of grains and

- 969 crystals in rocks. *Contributions to Mineralogy and Petrology*, 125, 60–74.
- 970 Jerram, D.A., Cheadle, M., and Philpotts, A.R. (2003) Quantifying the building blocks of igneous rocks:
971 are clustered crystal frameworks the foundation? *Journal of Petrology*, 44, 2033–2051.
- 972 Jerram, D.A., and Higgins, M.D. (2007) 3D analysis of rock textures: quantifying igneous microstructures.
973 *Elements*, 3, 239–245.
- 974 Johannes, W. (1984) Beginning of melting in the granite system Qz-Or-Ab-An-H₂O. *Contributions to*
975 *Mineralogy and Petrology*, 86, 264–273.
- 976 Johannes, W., and Holtz, F. (1996) *Petrogenesis and experimental petrology of granitic rocks*, 335 p.
977 Springer.
- 978 John, B.E., and Blundy, J.D. (1993) Emplacement-related deformation of granitoid magmas, southern
979 Adamello Massif, Italy. *Geological Society of America Bulletin*, 105, 1517–1541.
- 980 John, B.E., and Stünitz, H. (1997) Magmatic fracturing and small-scale melt segregation during pluton
981 emplacement: Evidence from the Adamello massif (Italy). In J.L. Bouchez, D.H.W. Hutton, and
982 W.E. Stephens, Eds., *Granite: From Segregation of Melt to Emplacement Fabrics* pp. 55–74.
983 Springer.
- 984 Kagami, H., Ulmer, P., Hansmann, W., Dietrich, V., and Steiger, R.H. (1991) Nd-Sr isotopic and
985 geochemical characteristics of the southern Adamello (northern Italy) intrusives: Implications for
986 crustal versus mantle origin. *Journal of Geophysical Research: Solid Earth*, 96, 14331–14346.
- 987 Kesley, C.H. (1965) Calculation of the CIPW norm. *Mineralogical Magazine*, 34, 376–282.
- 988 Lapworth, T., Wheeler, J., and Prior, D.J. (2002) The deformation of plagioclase investigated using
989 electron backscatter diffraction crystallographic preferred orientation data. *Journal of Structural*
990 *Geology*, 24.2, 387–399.
- 991 Laubscher, H.P. (1983) The late Alpine (Periadriatic) intrusions and the Insubric line. *Mem Soc Geol It*,
992 26, 21–30.
- 993 Launeau, P., Archanjo, C.J., Picard, D., Arbaret, L., and Robin, P. (2010) Two- and three-dimensional
994 shape fabric analysis by the intercept method in grey levels. *Tectonophysics*, 492.1, 230–239.
- 995 Launeau, P., and Robin, P.-Y.F. (1996) Fabric analysis using the intercept method. *Tectonophysics*, 267,
996 91–119.
- 997 Lee, C.T.A., and Morton, D.M. (2015) High silica granites: Terminal porosity and crystal settling in
998 shallow magma chambers. *Earth and Planetary Science Letters*, 409, 23–31.
- 999 Leuthold, J., Müntener, O., Baumgartner, L.P., and Putlitz, B. (2014) Petrological Constraints on the
1000 Recycling of Mafic Crystal Mushes and Intrusion of Braided Sills in the Torres del Paine Mafic
1001 Complex (Patagonia). *Journal of Petrology*, 55, 917–949.
- 1002 Liebske, C. (2015) *iSpectra: An Open Source Toolbox For The Analysis of Spectral Images Recorded on*
1003 *Scanning Electron Microscopes*. *Microscopy and Microanalysis*, 21, 1006–1016.
- 1004 Lipman, P.W. (2007) Incremental assembly and prolonged consolidation of Cordilleran magma chambers:

- 1005 Evidence from the Southern Rocky Mountain volcanic field. *Geosphere*, 3, 42.
- 1006 Lipman, P.W., and Bachmann, O. (2015) Ignimbrites to batholiths: Integrating perspectives from
1007 geological, geophysical, and geochronological data. *Geosphere*, 11, 1–39.
- 1008 Macera, P., Ferrara, G., Pescia, A., and Callegari, E. (1983) A geochemical study on the acid and basic
1009 rocks of the Adamello batholith. *Mem Soc Geol Ital*, 26, 223–259.
- 1010 Mainprice, D., Bachmann, F., Hielscher, R., and Schaeben, H. (2014) Descriptive tools for the analysis of
1011 texture projects with large datasets using MTEX: strength, symmetry and components. In D.R.
1012 Faulkner, E. Mariani, and J. Mecklenburgh, Eds., *Rock Deformation from Field, Experiments and*
1013 *Theory: A Volume in Honour of Ernie Rutter Vol. 8*. Geological Society, London.
- 1014 Martel, C., Pichavant, M., Holtz, F., Scaillet, B., Bourdier, J.-L., and Traineau, H. (1999) Effects of fO₂
1015 and H₂O on andesite phase relations between 2 and 4 kbar. *Journal of Geophysical Research:*
1016 *Solid Earth*, 104, 29453–29470.
- 1017 Martin, S., and Macera, P. (2014) Tertiary volcanism in the Italian Alps (Giudicarie fault zone, NE Italy):
1018 insight for double alpine magmatic arc. *Italian Journal of Geosciences*, 133, 63–84.
- 1019 Mauler, A., Godard, G., and Kunze, K. (2001) Crystallographic fabrics of omphacite, rutile and quartz in
1020 Vendée eclogites (Armorican Massif, France). Consequences for deformation mechanisms and
1021 regimes. *Tectonophysics*, 342.1, 81–112.
- 1022 Mayer, A., Cortiana, G., Dal Piaz, G.V., Deloule, E., De Pieri, R., and Jobstraibizer, P. (2003) U-Pb single
1023 zircon ages of the Adamello batholith, Southern Alps. *Mem. Sci. Geol*, 55, 151–167.
- 1024 McCarthy, T.S., and Groves, D.I. (1979) The Blue Tier Batholith, northeastern Tasmania. *Contributions to*
1025 *Mineralogy and Petrology*, 71.2, 193–209.
- 1026 McKenzie, D. (1984) The generation and compaction of partially molten rock. *Journal of Petrology*, 25,
1027 713–765.
- 1028 ——— (1985) The extraction of magma from the crust and mantle. *Earth and Planetary Science Letters*,
1029 74, 81–91.
- 1030 Meurer, W.P., and Boudreau, A.E. (1998a) Compaction of igneous cumulates part I: geochemical
1031 consequences for cumulates and liquid fractionation trends. *The Journal of geology*, 106, 281–
1032 292.
- 1033 ——— (1998b) Compaction of igneous cumulates part II: compaction and the development of igneous
1034 foliations. *The Journal of geology*, 106, 293–304.
- 1035 Miller, C.F., and Miller, J.S. (2002) Contrasting stratified plutons exposed in tilt blocks, Eldorado
1036 Mountains, Colorado River Rift, NV, USA. *Lithos*, 61, 209–224.
- 1037 Miller, C.F., Watson, E.B., and Harrison, T.M. (1988) Perspectives on the source, segregation and
1038 transport of granitoid magmas. *Earth and Environmental Science Transactions of the Royal*
1039 *Society of Edinburgh*, 79, 135–156.
- 1040 Mills, R.D., and Coleman, D.S. (2013) Temporal and chemical connections between plutons and
1041 ignimbrites from the Mount Princeton magmatic center. *Contributions to Mineralogy and*

- 1042 Petrology, 165, 961–980.
- 1043 Müller, A., van den Kerkhof, A.M., Behr, H.J., Kronz, A., and Koch-Müller, M. (2010) The evolution of
1044 late-Hercynian granites and rhyolites documented by quartz—a review. Geological Society of
1045 America Special Papers, 472, 185-204.
- 1046 Müller, A., Wiedenbeck, M., van den Kerkhof, A.M., Kronz, A., and Simon, K. (2003) Trace elements in
1047 quartz—a combined electron microprobe, secondary ion mass spectrometry, laser-ablation ICP-MS,
1048 and cathodoluminescence study. European Journal of Mineralogy, 15.4, 747-763.
- 1049 Namur, O., and Charlier, B. (2012) Efficiency of compaction and compositional convection during mafic
1050 crystal mush solidification: the Sept Îles layered intrusion, Canada. Contributions to Mineralogy
1051 and Petrology, 163, 1049–1068.
- 1052 Nandedkar, R. (2014) Evolution of hydrous mantle-derived calc-alkaline liquids by fractional
1053 crystallization at 0.7 and 0.4 GPa - An experimental study. PhD thesis, ETH Zürich.
- 1054 Nicolas, A. (1992) Kinematics in magmatic rocks with special reference to gabbros. Journal of Petrology,
1055 33.4, 891-915.
- 1056 Otamendi, J.E., Tiepolo, M., Walker, B.A., Cristofolini, E.A., and Tibaldi, A.M. (2016) Trace elements in
1057 minerals from mafic and ultramafic cumulates of the central Sierra de Valle Fértil, Famatinian arc,
1058 Argentina. Lithos, 240, 355-370.
- 1059 Paterson, S.R., Okaya, D., Memeti, V., Economos, R., and Miller, R.B. (2011) Magma addition and flux
1060 calculations of incrementally constructed magma chambers in continental margin arcs: Combined
1061 field, geochronologic, and thermal modeling studies. Geosphere, 7, 1439–1468.
- 1062 Paterson, S.R., Vernon, R.H., and Tobisch, O.T. (1989) A review of criteria for the identification of
1063 magmatic and tectonic foliations in granitoids. Journal of structural geology, 11, 349–363.
- 1064 Pennacchioni, G., Di Toro, G., Brack, P., Menegon, L., and Villa, I.M. (2006) Brittle–ductile–brittle
1065 deformation during cooling of tonalite (Adamello, Southern Italian Alps). Tectonophysics, 427,
1066 171–197.
- 1067 Perugini, D., De Campos, C.P., Ertel-Ingrisch, W., and Dingwell, D.B. (2012) The space and time
1068 complexity of chaotic mixing of silicate melts: implications for igneous petrology. Lithos, 155,
1069 326-340.
- 1070 Perugini, D., Poli, G., and Valentini, L. (2005) Strange attractors in plagioclase oscillatory zoning:
1071 petrological implications. Contributions to Mineralogy and Petrology, 149.4, 482-497.
- 1072 Petford, N. (2003) Rheology of Granitic Magmas During Ascent and Emplacement. Annual Review of
1073 Earth and Planetary Sciences, 31, 399–427.
- 1074 Philpotts, A.R., Brustman, C.M., Shi, J., Carlson, W.D., and Denison, C. (1999) Plagioclase-chain
1075 networks in slowly cooled basaltic magma. American Mineralogist, 84, 1819–1829.
- 1076 Philpotts, A.R., Carroll, M., and Hill, J.M. (1996) Crystal-Mush Compaction and the Origin of Pegmatitic
1077 Segregation Sheets in a Thick Flood-Basalt Flow in the Mesozoic Hartford Basin, Connecticut.
1078 Journal of Petrology, 37, 811–836.

- 1079 Philpotts, A.R., and Philpotts, D.E. (2005) Crystal-mush compaction in the Cohasset flood-basalt flow,
1080 Hanford, Washington. *Journal of Volcanology and Geothermal Research*, 145, 192–206.
- 1081 Philpotts, A.R., Shi, J., and Brustman, C. (1998) Role of plagioclase crystal chains in the differentiation of
1082 partly crystallized basaltic magma. *Nature*, 395, 343–346.
- 1083 Pistone, M., Arzilli, F., Dobson, K.J., Cordonnier, B., Reusser, E., Ulmer, P., Marone, F., Whittington,
1084 A.G., Mancini, L., Fife, J.L., and others (2015) Gas-driven filter pressing in magmas: Insights into
1085 in-situ melt segregation from crystal mushes. *Geology*, 43, 699–702.
- 1086 Piwinskii, A.J. (1968) Experimental Studies of Igneous Rock Series Central Sierra Nevada Batholith,
1087 California. *The Journal of Geology*, 76, 548–570.
- 1088 ——— (1973) Experimental studies of granitoids from the Central and Southern Coast Ranges,
1089 California. *Tschermaks mineralogische und petrographische Mitteilungen*, 20, 107–130.
- 1090 Piwinskii, A.J., and Wyllie, P.J. (1968) Experimental studies of igneous rock series: a zoned pluton in the
1091 Wallowa batholith, Oregon. *The Journal of Geology*, 76, 205–234.
- 1092 Prior, D.J., Boyle, A.P., Brenker, F., Cheadle, M.C., Day, A., Lopez, G., Peruzzo, L., Potts, G.J., Reddy,
1093 S., Spiess, R., and others (1999) The application of electron backscatter diffraction and orientation
1094 contrast imaging in the SEM to textural problems in rocks. *American Mineralogist*, 84, 1741–
1095 1759.
- 1096 Putirka, K.D., Canchola, J., Rash, J., Smith, O., Torrez, G., Paterson, S.R., and Ducea, M.N. (2014) Pluton
1097 assembly and the genesis of granitic magmas: Insights from the GIC pluton in cross section,
1098 Sierra Nevada Batholith, California. *American Mineralogist*, 99, 1284–1303.
- 1099 Reubi, O., and Blundy, J. (2009) A dearth of intermediate melts at subduction zone volcanoes and the
1100 petrogenesis of arc andesites. *Nature*, 461, 1269–1273.
- 1101 Sahagian, D.L., and Proussevitch, A.A. (1998) 3D particle size distributions from 2D observations:
1102 stereology for natural applications. *Journal of Volcanology and Geothermal Research*, 84, 173–
1103 196.
- 1104 Scaillet, B., and Evans, B.W. (1999) The 15 June 1991 Eruption of Mount Pinatubo. I. Phase Equilibria
1105 and Pre-eruption P–T–fO₂–fH₂O Conditions of the Dacite Magma. *Journal of Petrology*, 40, 381–
1106 411.
- 1107 Schaltegger, U., Brack, P., Ovtcharova, M., Peytcheva, I., Schoene, B., Stracke, A., Marocchi, M., and
1108 Bargossi, G. (2009) Zircon and titanite recording 1.5 million years of magma accretion,
1109 crystallization and initial cooling in a composite pluton (southern Adamello batholith, northern
1110 Italy). *Earth and Planetary Science Letters*, 286.1, 208–218.
- 1111 Schmidt, M.W., and Thompson, A.B. (1996) Epidote in calcalkaline magmas; an experimental study of
1112 stability, phase relationships, and the role of epidote in magmatic evolution. *American
1113 Mineralogist*, 81, 462–474.
- 1114 Schoene, B., Schaltegger, U., Brack, P., Latkoczy, C., Stracke, A., and Günther, D. (2012) Rates of
1115 magma differentiation and emplacement in a ballooning pluton recorded by U–Pb TIMS-TEA,
1116 Adamello batholith, Italy. *Earth and Planetary Science Letters*, 355–356, 162–173.

- 1117 Schwartz, A.J., Kumar, M., Adams, B.L., and Field, D.P., Eds. (2009) Electron Backscatter Diffraction in
1118 Materials Science. Springer US, Boston, MA.
- 1119 Schwindinger, K.R., and Anderson, A.T.J. (1989) Synneusis of Kilauea Iki olivines. Contributions to
1120 Mineralogy and Petrology, 103.2, 187–198.
- 1121 Shirley, D.N. (1986) Compaction of igneous cumulates. The Journal of Geology, 795–809.
- 1122 Sisson, T.W., and Bacon, C.R. (1999) Gas-driven filter pressing in magmas. Geology, 27, 613.
- 1123 Skemer, P., Katayama, I., Jiang, Z., and Karato, S.I. (2005) The misorientation index: Development of a
1124 new method for calculating the strength of lattice-preferred orientation. Tectonophysics, 411.1,
1125 157–167.
- 1126 Slaby, E., De Campos, C.P., Majzner, K., Simon, K., Gros, K., Moszumańska, I., and Jokubauskas, P.
1127 (2016) Feldspar megacrysts from the Santa Angélica composite pluton —
1128 Formation/transformation path revealed by combined CL, Raman and LA-ICP-MS data. Lithos.
- 1129 Slaby, E., and Götze, J. (2004) Feldspar crystallization under magma-mixing conditions shown by
1130 cathodoluminescence and geochemical modelling—a case study from the Karkonosze pluton (SW
1131 Poland). Mineralogical Magazine, 68.4, 561–577.
- 1132 Spera, F.J., Oldenburg, C.M., Christensen, C., and Todesco, M. (1995) Simulations of convection with
1133 crystallization in the system $\text{KAlSi}_2\text{O}_6\text{-CaMgSi}_2\text{O}_6$: Implications for compositionally zoned
1134 magma bodies. American Mineralogist, 80.11–12, 1188–1207.
- 1135 Streck, M.J. (2014) Evaluation of crystal mush extraction models to explain crystal-poor rhyolites. Journal
1136 of Volcanology and Geothermal Research, 284, 79–94.
- 1137 Streck, M.J., and Grunder, A.L. (2007) Phenocryst-poor rhyolites of bimodal, tholeiitic provinces: the
1138 Rattlesnake Tuff and implications for mush extraction models. Bulletin of Volcanology, 70, 385–
1139 401.
- 1140 Tappa, M.J., Coleman, D.S., Mills, R.D., and Samperton, K.M. (2011) The plutonic record of a silicic
1141 ignimbrite from the Latir volcanic field, New Mexico. Geochemistry, Geophysics, Geosystems,
1142 12, Q10011.
- 1143 Taylor, H.P. (1980) The effects of assimilation of country rocks by magmas on $^{18}\text{O}/^{16}\text{O}$ and $^{87}\text{Sr}/^{86}\text{Sr}$
1144 systematics in igneous rocks. Earth and Planetary Science Letters, 47, 243–254.
- 1145 Tegner, C., Thy, P., Holness, M.B., Jakobsen, J.K., and Leshner, C.E. (2009) Differentiation and
1146 Compaction in the Skaergaard Intrusion. Journal of Petrology, 50, 813–840.
- 1147 Thompson, A.B., Matile, L., and Ulmer, P. (2002) Some thermal constraints on crustal assimilation during
1148 fractionation of hydrous, mantle-derived magmas with examples from central Alpine batholiths.
1149 Journal of Petrology, 43.3, 403–422.
- 1150 Tiepolo, M., Tribuzio, R., and Langone, A. (2011) High-Mg andesite petrogenesis by amphibole
1151 crystallization and ultramafic crust assimilation: evidence from Adamello hornblendites (Central
1152 Alps, Italy). Journal of Petrology, 52.5, 1011–1045.
- 1153 Tuttle, O.F., and Bowen, N.L. (1958) Origin of granite in the light of experimental studies in the system

- 1154 NaAlSi₃O₈–KAlSi₃O₈–SiO₂–H₂O. Geological Society of America Memoirs, 74, 1-146.
- 1155 Turnbull, R., Weaver, S., Tulloch, A., Cole, J., Handler, M., and Ireland, T. (2010) Field and Geochemical
1156 Constraints on Mafic–Felsic Interactions, and Processes in High-level Arc Magma Chambers: an
1157 Example from the Halfmoon Pluton, New Zealand. *Journal of Petrology*, 51, 1477–1505.
- 1158 Ulmer, P., Callegari, E., and Soderegger, U.C. (1983) Genesis of the mafic and ultramafic rocks and their
1159 genetical relations to the tonalitic-trondhjemitic granitoids of the southern part of the Adamello
1160 batholith (Northern Italy). *Mem Soc Geol Ital*, 26, 171–222.
- 1161 Vance, J.A. (1969) On synneusis. *Contributions to Mineralogy and Petrology*, 24, 7–29.
- 1162 Vasyukova, O.V., Kamenetsky, V.S., Goemann, K., and Davidson, P. (2013) Diversity of primary CL
1163 textures in quartz from porphyry environments: implication for origin of quartz eyes.
1164 *Contributions to Mineralogy and Petrology*, 166.4, 1253-1268.
- 1165 Vigneresse, J.L., Barbey, P., and Cuney, M. (1996) Rheological Transitions During Partial Melting and
1166 Crystallization with Application to Felsic Magma Segregation and Transfer. *Journal of Petrology*,
1167 37, 1579–1600.
- 1168 Vollmer, F.W. (1990) An application of eigenvalue methods to structural domain analysis. *Geological
1169 Society of America Bulletin*, 102, 786–791.
- 1170 von Platen, H. (1965) Kristallisation granitischer Schmelzen. *Beiträge zur Mineralogie und Petrographie*,
1171 11, 334–381.
- 1172 Wager, L.R. (1960) The major element variation of the layered series of the Skaergaard intrusion and a
1173 re-estimation of the average composition of the hidden layered series and of the successive
1174 residual magmas. *Journal of Petrology*, 1.3, 364–398.
- 1175 Wager, L.R., and Brown, G.M. (1968) Layered igneous rocks. Oliver & Boyd, Edinburgh.
- 1176 Walker, B.A., Bergantz, G.W., Otamendi, J.E., Ducea, M.N., and Cristofolini, E.A. (2015) A MASH Zone
1177 Revealed: the Mafic Complex of the Sierra Valle Fértil. *Journal of Petrology*, 56, 1863–1896.
- 1178 Weinberg, R.F. (2006) Melt segregation structures in granitic plutons. *Geology*, 34, 305–308.
- 1179 Wheeler, J., Prior, D., Jiang, Z., Spiess, R., and Trimby, P. (2001) The petrological significance of
1180 misorientations between grains. *Contributions to Mineralogy and Petrology*, 141.1, 109–124.
- 1181 Wickham, S.M. (1987) The segregation and emplacement of granitic magmas. *Journal of the Geological
1182 Society*, 144, 281–297.
- 1183 Wiebe, R.A., Wark, D.A., and Hawkins, D.P. (2007) Insights from quartz cathodoluminescence zoning
1184 into crystallization of the Vinalhaven granite, coastal Maine. *Contributions to Mineralogy and
1185 Petrology*, 154.4, 439-453.
- 1186 Žák, J., Verner, K., and Týcová, P. (2008) Grain-scale processes in actively deforming magma mushes:
1187 New insights from electron backscatter diffraction (EBSD) analysis of biotite schlieren in the
1188 Jizera granite, Bohemian Massif. *Lithos*, 106.3, 309-322.
- 1189

1190

List of figure captions

1191

1192 **Figure 1** (a) The four superunits of the Adamello batholith, wedged between the Tonale and
1193 Giudicarie lines. Simplified geological map after Schaltegger et al. (2009), modified from
1194 Schoene et al. (2012). (b) The Lago della Vacca complex with its four main units Val Fredda,
1195 Blumone (including the "Avortici" and "Spotty Dog" batches), Vacca, and Galliner. Simplified
1196 geological map with foliation orientations after John and Blundy (1993), modified from Schoene
1197 et al. (2012). Sampling locations are indicated with yellow stars. * Blumone Complex after Brack
1198 (1983) and Ulmer et al. (1983); ** Lago della Vacca Suite after John and Blundy (1993).
1199 Sampling areas indicated with rectangles

1200 **Figure 2** Field observations: (a) flattened mafic enclaves in foliated Re di Castello quartz diorite;
1201 (b) leucocratic segregation band, exhibiting variable thickness and lack of amphibole and biotite,
1202 in Western Adamello tonalite. The transition from leucocratic band to homogeneous tonalite is
1203 not sharp. The homogeneous tonalite contains randomly oriented, large hornblende crystals, and
1204 clots of dark minerals or mafic enclaves

1205 **Figure 3** Diagram of (a) Rb versus SiO₂ concentrations and (b) Sr versus SiO₂ concentration
1206 from database (Macera et al. 1983; Blundy and Sparks 1992 and unpublished theses from Brack
1207 1980; Schellhorn 1980; Sonderegger 1980; Ulmer 1982; Stauffacher 2012; Bôle 2012; Verbene
1208 2013; Fiedrich 2015). Data for the units Val Fredda (e.g. Broderick et al. 2015) and Lago della
1209 Vacca (including Blumone), are displayed as red and black symbols; data from the entire Re di
1210 Castello superunit (including enclaves, dikes, aplites, and pegmatites) are outlined by the red
1211 fields. Yellow stars represent compositions of samples Ada14-AV1a, -AV2, -AF14, -AF15 –
1212 from left to right with increasing SiO₂ content

1213 **Figure 4** Optical cathodoluminescence images of samples from WAT (a, d) and LdV (b, c).
1214 Green = plagioclase, black = amphibole, biotite, dark blue = quartz, turquoise = alkali feldspar,
1215 yellow = apatite, dark green = chloritized biotite. (a) overview image showing phase relations; (b)
1216 plagioclase cluster with dark green rim; (c) quartz with variable luminescence brightness; (d)
1217 myrmekite between zoned plagioclase and alkali feldspar

1218 **Figure 5** Combined phase and plagioclase maps based on SEM-EDS element mapping for (a)
1219 sample Ada14-AV2 from LdV, section perpendicular to foliation, and (b) for sample
1220 Ada14-AF14 from WAT. Colors correspond to different phases and anorthite contents

1221 **Figure 6** (a) Inverse pole figure-color coded crystal orientation map of strongly foliated (and
1222 lineated) sample Ada14-AV1a from LdV. Predominant turquoise color of the plagioclase crystals
1223 indicates preferred orientation of the b-axes parallel to the short edge of the scan (perpendicular
1224 to the visible foliation). The long edge of the thin section was oriented parallel to visible
1225 foliation. Twins were excluded before crystals were outlined. Only plagioclase is displayed in
1226 color, all other phases are black. Plagioclase crystal orientation depicted by the three pole figures
1227 for crystallographic axes a [100], b [010] and c [001], displayed in equal area density
1228 distributions calculated on the basis of a harmonic ODF with Mtex. Grains smaller than 5 pixels
1229 were removed. (b) Crystal orientation map of a sample that is rich in trapped liquid, Ada14-AF15
1230 from WAT. No predominant color indicates lack of preferred alignment of crystals with respect
1231 to the thin section short edge. Three pole figures show random orientations

1232

1233 **Figure 7** Quantification of CPO with the Point-Girdle-Random (PGR) method after Mainprice et
1234 al. (2014) and Vollmer (1990). The calculation was done for each crystallographic axis
1235 separately, resulting in three triangles. Samples at the blue end of the color bar have a smaller

1236 amount of “minimum trapped melt” (t.m.) then those at the yellow end. * The leucocratic part of
1237 this sample (Ada14-AF16) was analyzed

1238

1239 **Figure 8** Bent plagioclase crystal of sample Ada14-AV1a from LdV: (a) misorientation map:
1240 color coding corresponds to misorientation angle with respect to reference point (star), and
1241 reveals significant intracrystalline deformation; (b) polarized light microscopic image: Bending
1242 of the crystal is reflected in undulose extinction, lamellar deformation twins, and faint kinks; (c)
1243 upper hemisphere, equal-angle stereographic projections of the three axes a [100], b [010], and c
1244 [001]. Rotation of the b- and c-axes about the a-axis is visible

1245

1246 **Figure 9** Melt extraction and development of CPO in the crystallizing magma chamber. Color
1247 variation indicates change of melt composition, and formation of new crystals and overgrowth
1248 rims (grey), by fractional crystallization. Volume decrease from early to late stage indicates melt
1249 extraction. Early stage: Free-floating crystals before the rheological lock-up. Intermediate stage
1250 (main melt extraction window): The rheological lock-up is reached, a foliation develops, and melt
1251 is lost. The remaining melt at this stage corresponds to the “maximum trapped liquid”. Late
1252 stage: At high crystallinity, compaction supposedly dominates melt extraction and is indicated by
1253 crystal bending. The remaining interstitial melt at this stage corresponds to the “minimum
1254 trapped liquid”

1255

1256

Tables

1257 **Table 1** Phase proportions (in area% or volume%, see text) as determined from EDS scans.
1258 Samples in rows 1-6 from LdV, in rows 7-9 from WAT

	Qz	Afs	Pl ^a	Pl ^b	Hbl	Bt+Chl	FeOx+Ttn	Unind.
AV1a ^c	7	2	20	41	23	1	2	4
AV2.i ^c	15	2	23	36	14	6	1	3
AV2.ii ^c	14	2	22	32	21	6	1	3
AV2.iii ^c	12	2	22	37	17	5	2	3
SD2 ^c	11	2	21	38	17	7	2	3
VA3 ^c	23	2	12	39	5	14	1	5
AF14.1 ^{d,f}	22	5	17	37	5	12	0	3
AF15.1 ^d	29	6	16	24	11	12	1	2
AF16a3 ^d	35	7	26	27	0	3	0	2

1259 Pl^a: plagioclase with anorthite \leq 40; Pl^b: plagioclase with $>$ 40; Unind. = unindexed pixels and
 1260 accessory phases; ^d samples from LdV; ^e samples from WAT; ^f The results for Ada14-AF14.1 are
 1261 averaged from two thin section scans

1262

1263 **Table 2** Estimates for the amounts of “minimum” and “maximum trapped melt”, based on phase
 1264 and plagioclase maps

	minimum trapped melt	maximum trapped melt
AV1a ^a	7	31
AV2.i ^a	15	46
AV2.ii ^a	14	44
AV2.iii ^a	12	41

SD2 ^a	11	41
VA3 ^a	23	50
AF14.1 ^b	22	55
AF15.1 ^b	29	62
AF16a3 ^b	35	71

1265 ^a samples from LdV; ^b samples from WAT

1266

1267

Electronic supplements

1268

1269 **Supplemental data file 1** Compilation of compositional data (major and trace elements; XRF
1270 and LA-ICP-MS, respectively) from the Adamello batholith. References listed within Excel file

1271

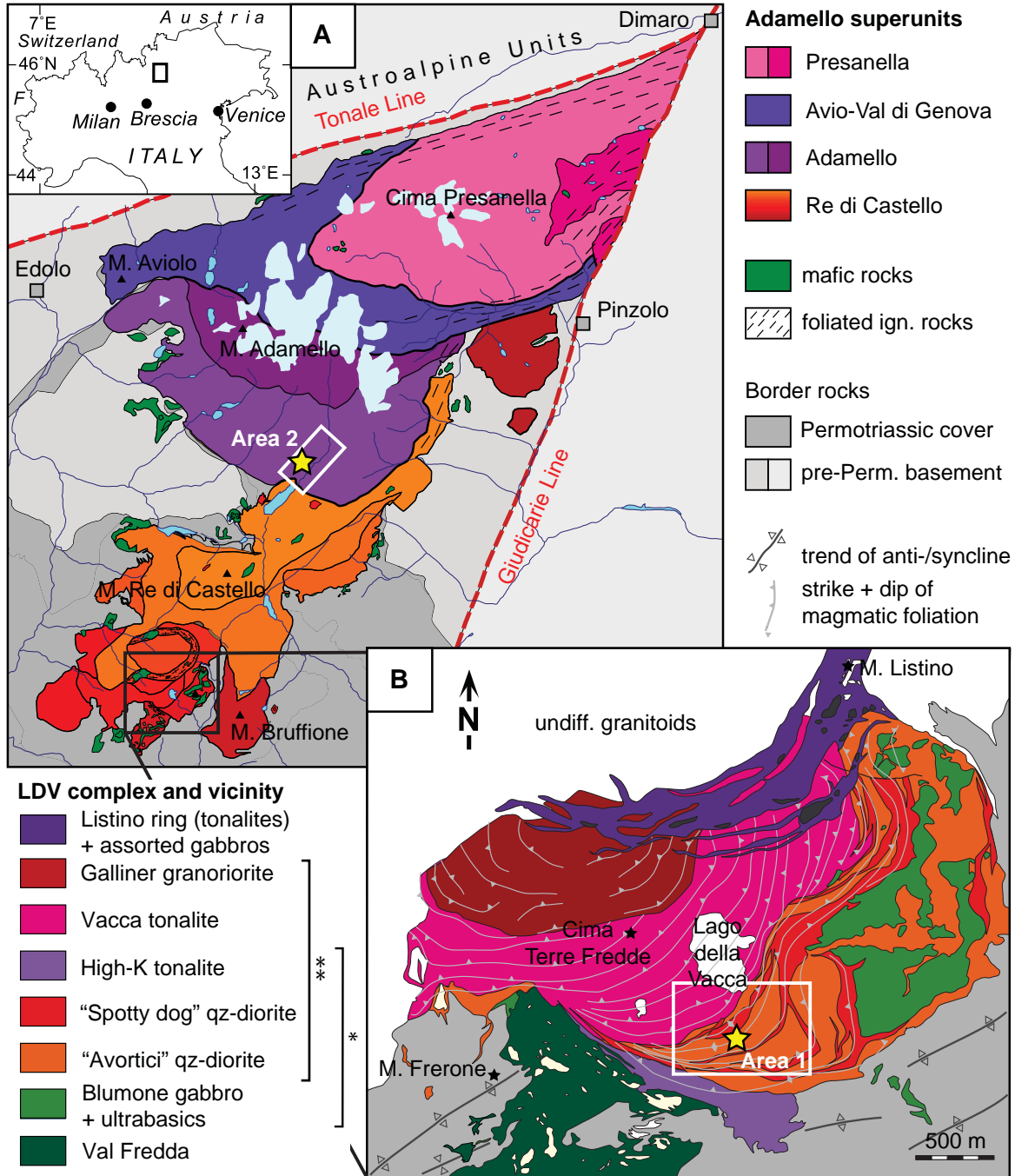
1272 **Supplemental data file 2** Plagioclase compositional profiles acquired with EPMA

1273

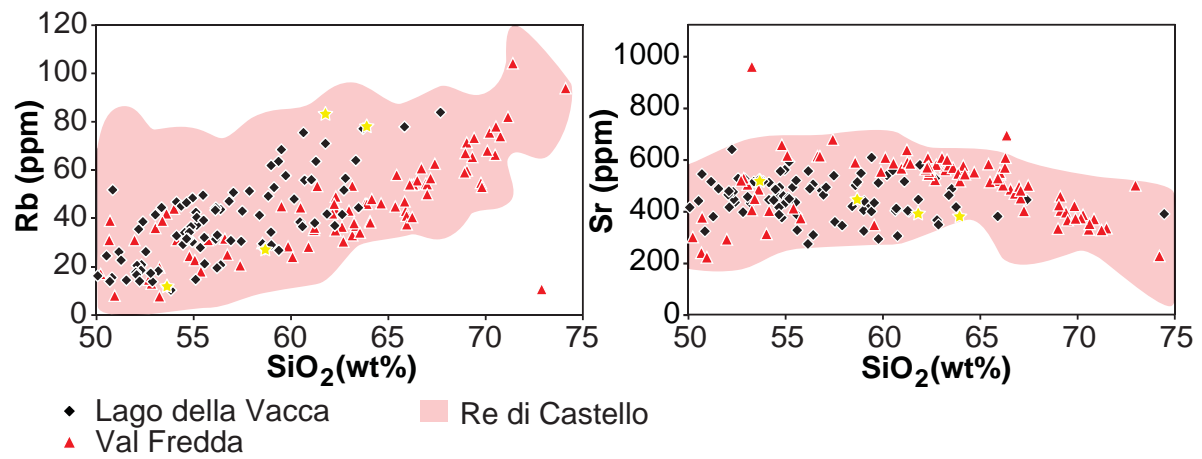
1274 **Supplemental data file 3** Major and trace element mass balance and CLF calculations

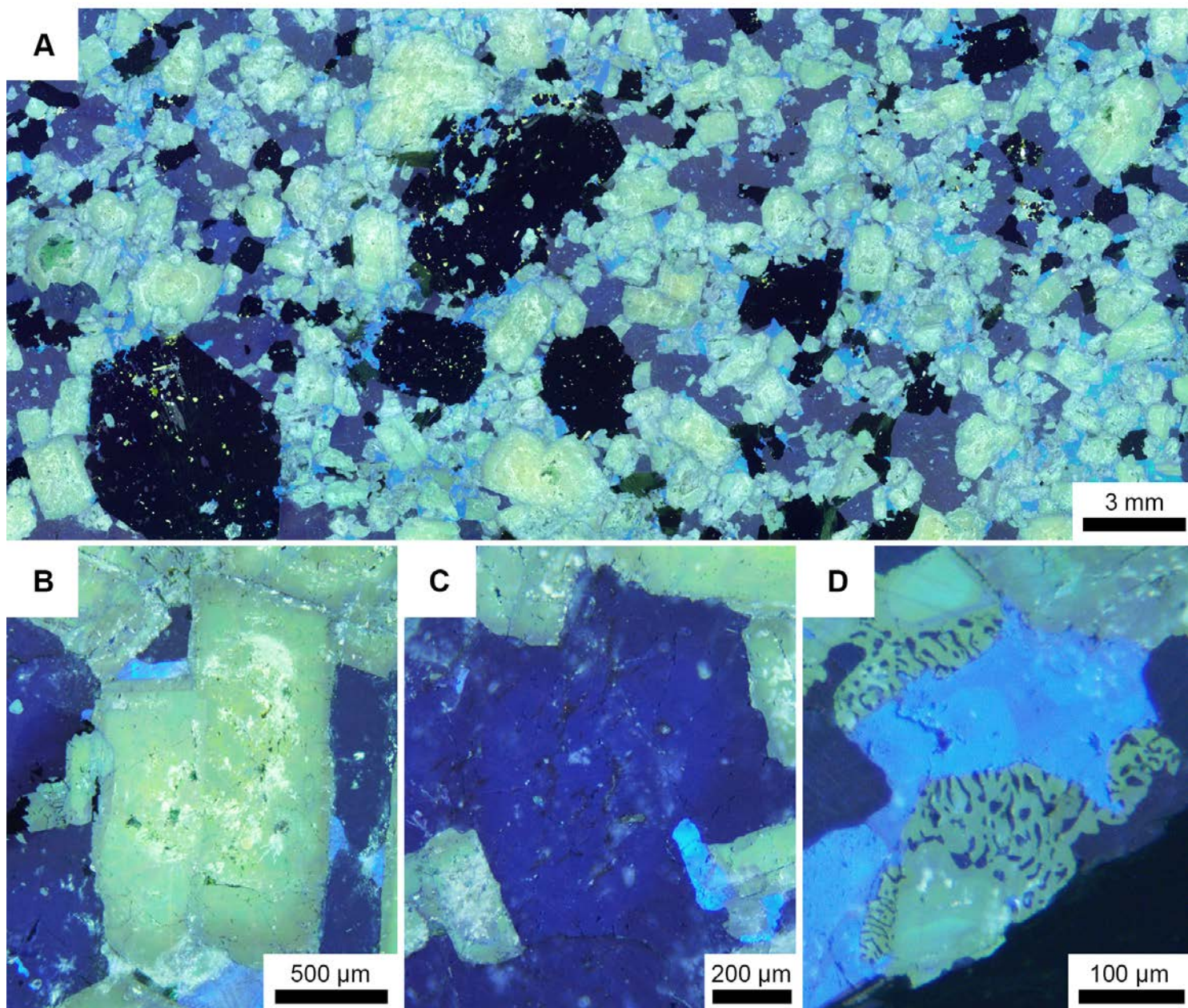
1275

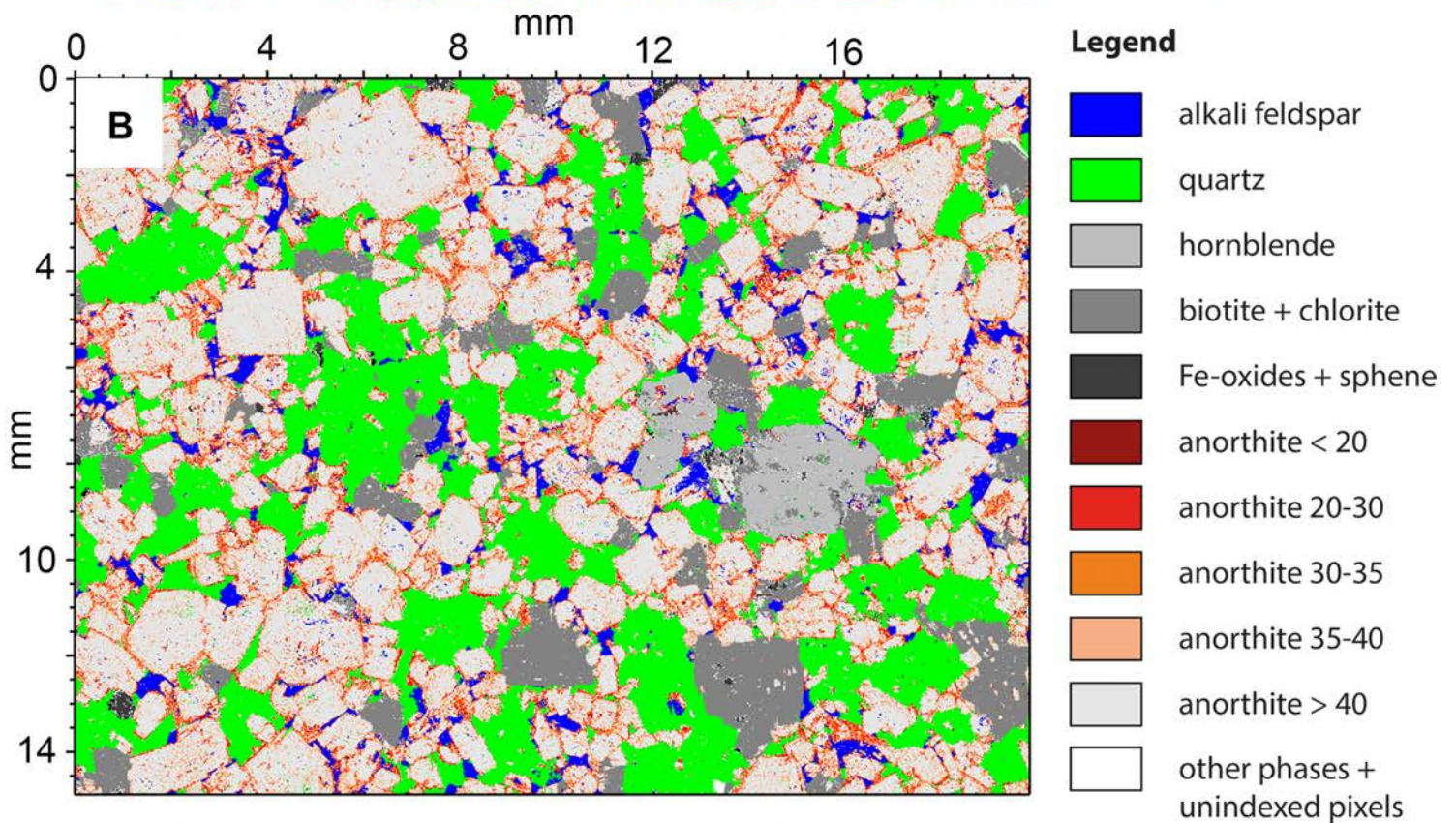
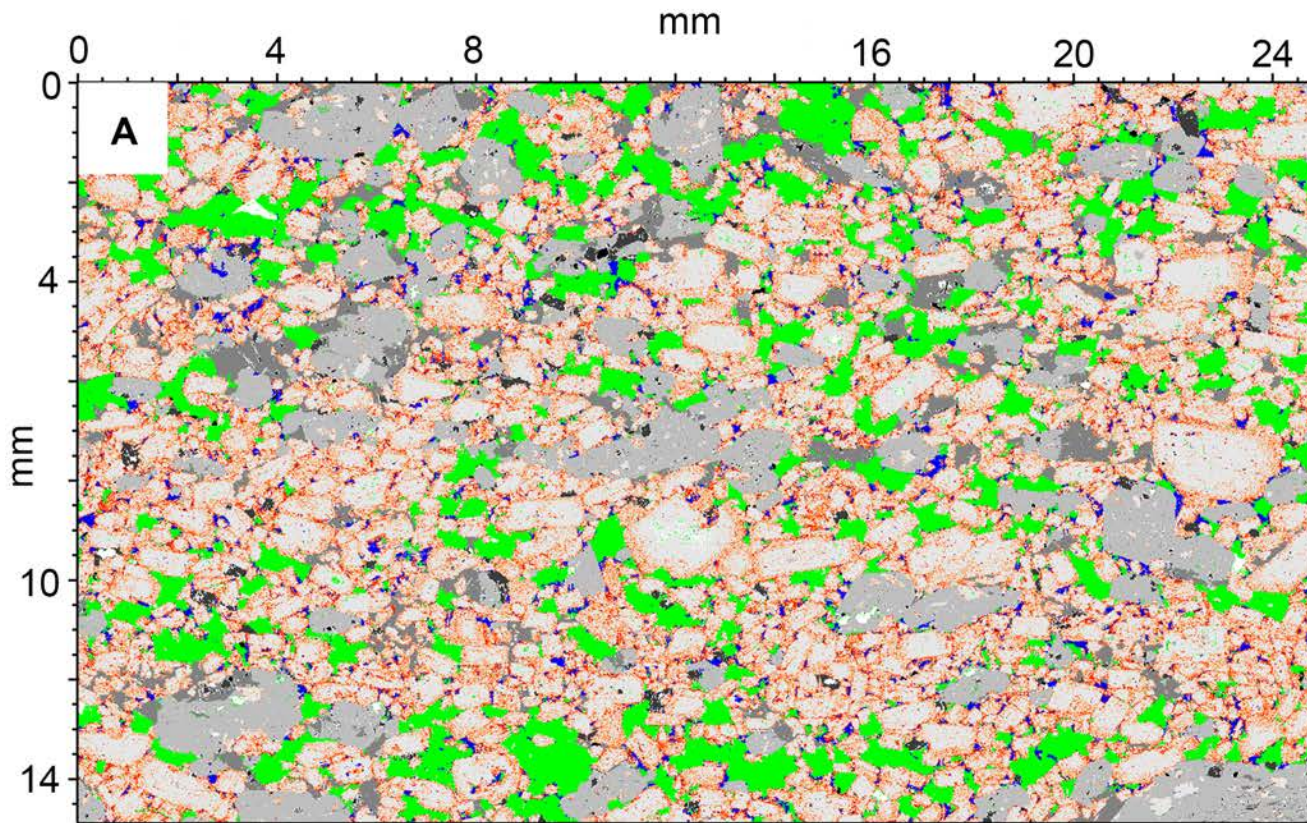
1276 **Supplemental data file 4** Thin section photos











6

